Modeling and Large Signal Stability Analysis of A DC/AC Microgrid

by

Hongru Xu

A Thesis Presented in Partial Fulfillment
of the Requirements for the Degree
Master of Science

Approved June 2018 by the
Graduate Supervisory Committee:

Yan Chen, Chair
Nathan Johnson
Qin Lei

ARIZONA STATE UNIVERSITY

August 2018

ABSTRACT

The concept of the microgrid is widely studied and explored in both academic and industrial societies. The microgrid is a power system with distributed generations and loads, which is intentionally planned and can be disconnected from the main utility grid. Nowadays, various distributed power generations (wind resource, photovoltaic resource, etc.) are emerging to be significant power sources of the microgrid.

This thesis focuses on the system structure of Photovoltaics (PV)-dominated microgrid, precisely modeling and stability analysis of the specific system. The grid-connected mode microgrid is considered, and system control objectives are: PV panel is working at the maximum power point (MPP), the DC link voltage is regulated at a desired value, and the grid side current is also controlled in phase with grid voltage. To simulate the real circuits of the whole system with high fidelity instead of doing real experiments, PLECS software is applied to construct the detailed model in chapter 2. Meanwhile, a Simulink mathematical model of the microgrid system is developed in chapter 3 for faster simulation and energy management analysis. Simulation results of both the PLECS model and Simulink model are matched with the expectations. Next chapter talks about state space models of different power stages for stability analysis utilization. Finally, the large signal stability analysis of a grid-connected inverter, which is based on cascaded control of both DC link voltage and grid side current is discussed. The large signal stability analysis presented in this thesis is mainly focused on the impact of the inductor and capacitor capacity and the controller parameters on the DC link stability region. A dynamic model with the cascaded control logic is proposed. One Lyapunov large-signal stability analysis tool is applied to derive the domain of attraction, which is the asymptotic stability region.

Results show that both the DC side capacitor and the inductor of grid side filter can significantly influence the stability region of the DC link voltage. PLECS simulation models developed for the microgrid system are applied to verify the stability regions estimated from the Lyapunov large signal analysis method.

ACKNOWLEDGMENTS

I would like to deeply thank my advisor Prof. Yan Chen at Arizona State University for advising me and giving me guidance and support. His professional understanding and special skills in research work helped me a lot in doing the research work. I also appreciate the help from my supervisory committee, Prof. Nathan Johnson, and Prof. Qin Lei.

I would like to thank the SRP company for supporting my research work. I want to thank my teammate Yue Zhao for the cooperative work, discussions, and suggestions. I would also like to thank the Ph.D. students in DSCL lab Fengchen Wang, Yiwen Huang, Ao Li for the support and help in teaching me some skills and giving me some personal understanding towards the research work using their major knowledge.

Finally, I would like to thank my parents Zhong Xu and Donglin Qian for supporting my living and studying in Arizona State University, giving me courage and confidence in the daily life whenever I encounter a hard time, I thank them from the bottom of my heart.

TABLE OF CONTENTS

CHAPTER

CHAPTER Page

APPENDIX

LIST OF TABLES

LIST OF FIGURES

Figure Page

Figure Page

Figure Page

1. INTRODUCTION

1.1 Background

Energy is the cornerstone of the existence and development of modern society. With the continuous development of the global economy and society, energy consumption has also been increasing in recent years. Consequently, the scarcity of fossil fuels has become an issue, which shows a significant challenge for the whole world. To alleviate the issue brought by the increasingly tense request and supply of fossil energy, the large-scale development and application of renewable energy have become an essential part of the energy strategies of various countries. For example, solar energy is an inexhaustible source of renewable energy. It has sufficient cleanliness, absolute safety, relative versatility, exact longevity and maintenance freeness, adequacy of resources, and potential economics. These advantages make solar energy an essential role in the long-term energy strategy.

To sufficiently and effectively utilize solar energy, PV (Photovoltaic) microgrid systems are playing an important role in renewable energy system nowadays. Many other renewable energy sources are gradually applied as well, for instance, wind energy and hydro energy. Electric power generated from different renewable energy sources can be directly used, which provides customers with various choices. Meanwhile, different renewable energy sources can work in parallel to improve the power quality and stability of the microgrid. As a result, the integration of PV panels and/or other (renewable energy) sources into the utility grid becomes necessary.

1.2 Literature review

The structure of Microgrid is still changing during these years. According to the standards IEEE 1547.4-2011 [1], the term DR (distributed resources) island systems that generally refer to Microgrid. Typically, microgrids are the EPS (Electric power systems) that: (1) can be disconnected from main utility grid under urgent circumstances, (2) have DR and load requirements, (3) are planned on purpose.

Under normal conditions, microgrid systems will always be connected to the main power system for stability and energy allocation concerns. There are also different control ways to manage the power flow and incorporation between the microgrid and main power systems. Talking about the main power system, the U.S power system [2] is an intensively sophisticated system of system, including the power generation, transmission, and distributed energy system. Moreover, a lot of functional institutions concerning planning, operating and supervision are related to the U.S power system. Last, end use and distributed energy resources are the critical parts of the power system as well.

The U.S power system comprises:

Generation: Electricity generation takes up to the most significant portion of the U.S. primary energy usage, among which the domestically produced coal accounts for 80%, one-third of the gas production, and almost all the nuclear and abiotic renewable energy production.

Transmission: The U.S. transmission network includes all the electrical power lines that connect power generators with the local power electric companies.

Distribution system: The reason for comprising larger size power system generators and transmission networks is to provide enough electricity to distribution substations stably. On the contrary, the distribution system is responsible for providing electricity at the desired time and place of the customer and fulfilling the minimum criteria of reliability and power quality at the same time.

Distributed energy resources (DERs): Distributed energy resources form a wide range of technologies, which significantly influence the power demand and time required by the power grid. Although there are different definitions of distributed energy resources, this term is applied in the Quadrennial Energy Review (QER) to specific include distributed generation, distributed energy storage, and technologies of power resource management on demand side. Moreover, the power efficiency is also one part of it.

End use: The infrastructure facility, which refers to use, demand or power transfer physical components, the function of which is to provide product or service to the consumers.

Primary distribution lines [3] are basically "medium-voltage" lines, normally considered from 600V to 35kV. In distribution substation, the substation transformers separate the input voltage (35to 230kV) to several distribution primary lines, then the substation sends all the energy out. Substation transformer will get the primary distribution voltage and degrades the primary voltage to lower secondary voltage circuits (Usually 120/240V, other voltage may also apply), then every end use consumers get access to such power electricity. Finally, the end use consumer is connected to the service port of substation transformer and secondary substation circuits.

In recent years, more and more distributed energy resources are becoming the supplement and substitution of large traditional central power plants. Distributed generations have the following popular technologies [4], which are increasingly applied in our life.

PV technology: with the improvement of research and analysis work of PV system, it is now regarded as the alternative energy or complementary energy source in either pure

PV system or hybrid system. It is suggested to increase the reliability, reasonable cost and user-friendly topologies design for making the PV system working more efficiently. In other words, to enhance the PV system performance as much as possible.

Wind turbine technology: In wind generation system, the technology has been developed to a mature level, which is ready for authentic, stable power generation method in a public facility. In the past recent years, wind turbine system technology had been through enormous change. From the rim of the technology in the 1970s to 2000s wind turbine generator, which implements the latest power electronics devices, air dynamics, and mechanical drive system design,

Energy storage system: the existence of the storage system in the renewable energy system is for supporting the reactive power required by load and other power electronic device. More importantly, the energy storage is used to maintain the DC link voltage stability in islanded microgrid working condition. Usually, Supercapacitors, battery bank, flywheels, and compressed air energy storage are applied to DC link connection for higher quality electricity generation.

Since the microgrid of this thesis is PV- dominated, the PV inverter system is introduced, which has the following classification: Usually, the PV inverter system is divided into three types: central inverters, micro-inverters, and string inverters. The basic schematic of central inverters is to connect PV modules in parallel, then the DC-DC boost converter and inverter is connected to the whole PV output. The micro-inverters idea is to make every single PV module connect to a specific inverter, which can accurately track the maximum power working point. However, the cost will be relatively high. The string inverters connect all the PV panels in one string and the output of which is connected to DC-DC boost converter cascaded with an inverter.

In general, PV inverter system can be classified into three parts [4]: PV panel, DC-DC boost converter, and inverter. Meanwhile, the isolated DC-DC converter or non-isolated DC-DC converter needs to be chosen. Frequency transformer is applied to fulfill galvanic isolation. The utilization of transformer is one of the necessary isolation (Required by U.S. regulation). Modern inverter inclines to be designed with a high-frequency transformer. However, the isolated DC-DC boost converter is not required to be installed in PV inverter system in some countries where the grid isolation is not mandatory.

PV inverter system operation conditions: Usually, PV inverter system working modes have two types: grid-connected and stand-alone respectively. Grid-connected mode means the inverter output side is connected to the utility grid through harmonics filter. Under this kind of total system configuration, the major power source is still from PV panel. When the power demand is higher than the maximum output power of PV panel, grid side will provide power. For stand-alone mode PV microgrid, the nominal energy source of the microgrid is the PV. Moreover, the energy storage presents an important role. The major difference between these two working modes is the control logic. Finally, the PV microgrid has single phase and three phase configurations.

The stability analysis should be taken into consideration before the microgrid system is applied into practical use. Usually, stability analysis problems of the power system are divided into three categories by IEEE/CIGRE united cooperation group. Rotor angle stability, voltage stability and frequency stability [16]. As for rotor angle stability, since there is no generator DG unit in the proposed system, it is not considered in this case. The basic idea is to maintain a specific angle to output stable power. Voltage stability refers to the ability of all the lines maintaining at a stable voltage in power system under disturbances. For this specific system in this thesis, the stable operating conditions are defined as stable dc link voltage, PV maximum power point tracking, grid side current in phase with the grid voltage, and the voltage and current ripple satisfies the requirement. Once all these requirements are fulfilled, the system is stable. It is the power balance between load demand and power supply on each bus. Frequency stability is the ability of the power system working in a stable frequency under all kinds of conditions. For instance, system frequency declines as the load added up; this is the balance between generation and load plus power loss. The voltage stability is related to reactive power, but the frequency stability has something to do with the active power. If there is a fluctuation in power grid frequency, the voltage will also be influenced.

Microgrid operation principles: Microgrid can operate in both grid-connected mode and islanded mode. Different control strategies can be applied to regulate the voltage and frequency. Microgrid has a much faster response time in fault situation due to small output impedance and small over-current capability.

Classification of Microgrid stability:

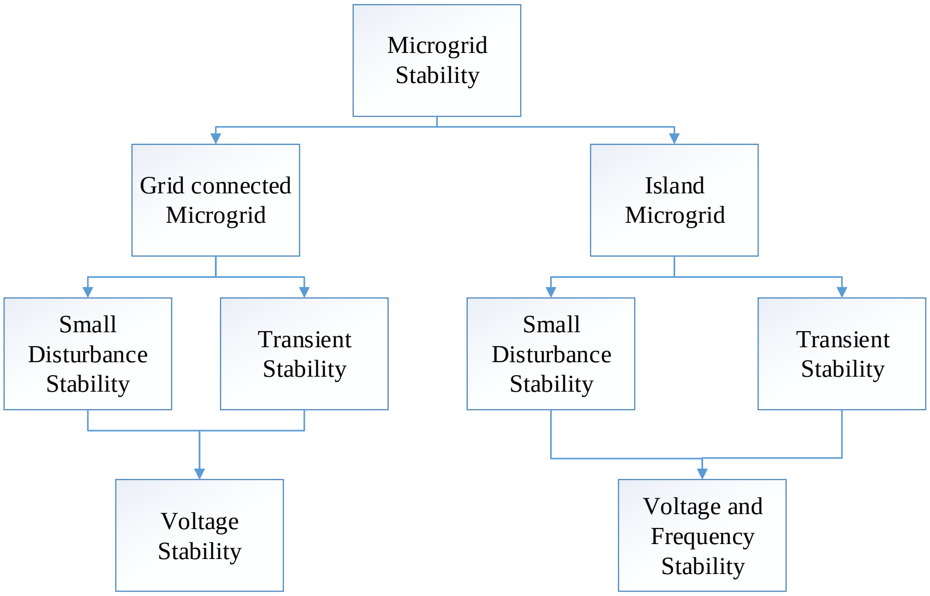

Figure 1. General Classification of Microgrid stability.
(Modified from [25])

For grid-connected microgrid. Small signal stability analysis mainly focuses on how the load disturbances and droop controller parameters impact the voltage stability of the total microgrid. A microgrid is usually not large, and the disturbance happened in it will not influence the frequency of utility grid. So, the rotor angle stability and frequency stability are not considered in the grid-connected microgrid. Another part of grid-connected stability is about transient stability, which is classified into short-term and super short-term transient. Because when there is a fault happens in grid side, the controller should respond in microseconds to overcome the threats of current flowing into an inverter, which will cause the safety issue of the microgrid.

Microgrid transient stability:

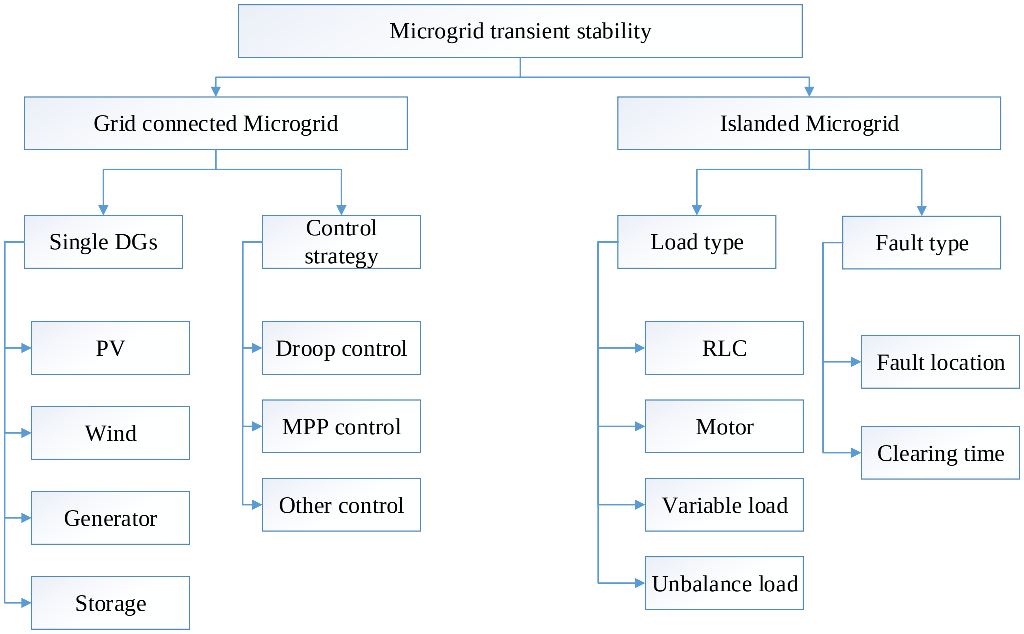

Figure 2. Microgrid transient stability.
(Modified from [25])

2. SINGLE PHASE GRID-TIED PV INVERTER SYSTEM WITH ENERGY STORAGE AND PEV

2.1 Introduction

Photovoltaic systems with high power stages are becoming more and more popular in recent years. The PV inverter system consists of photovoltaic energy source, converter, and the inverter that can be directly connected to the grid. For the proposed system in this thesis, there is also an energy storage system connected to the DC link. Besides, the PEV that represents an additional load is located at the AC side. Basically, the two working modes of the microgrid are grid-connected and stand-alone. Both modes can be analyzed separately and the difference between these two modes is the control strategy. For the grid-connected mode, PV system that is considered in this thesis will mainly power the AC load. When the demand is higher than the PV output power, the grid will support the power requirement. On the other hand, if the power of PV exceeds the requirements of the load, the remaining power will be absorbed in the energy storage device, in this thesis, which is the battery storage. Moreover, when there is a sudden load variation, the control strategy should shift from the MPPT mode to droop control model for frequency regulation. Once the frequency of the system is regulated by the droop controller, an external signal will drive the system to work at the MPPT mode to sufficiently utilize the PV module. The modeling, electric circuits, and component parameters extraction based on the grid-connected mode will be mainly discussed in this thesis.

2.2 System descriptions

PV inverter system is typically classified into two categories: single phase and three phase inverter system. Typically, the three-phase PV inverter system has more practical values. Considering the transmission and power generation issues, the three-phase power system is usually used because of cost-effective characteristics and lower loss during the transmission process. In the industrial and commercial fields, the utility system is also commonly connected to the three-phase PV inverter system. However, if the power rating of the system is lower than 10kW, the single-phase PV system is suitable. For a system with a larger power rating, the three-phase PV inverter system is safer and more economical. This thesis presents the detailed modeling of a specific single-phase PV inverter system for research purposes. In this type of single-phase PV inverter system, the HF (high-frequency) or LF (low-frequency) transformer is also needed in high voltage level systems for galvanic isolation.

The overview of the whole system is in Figure 3.

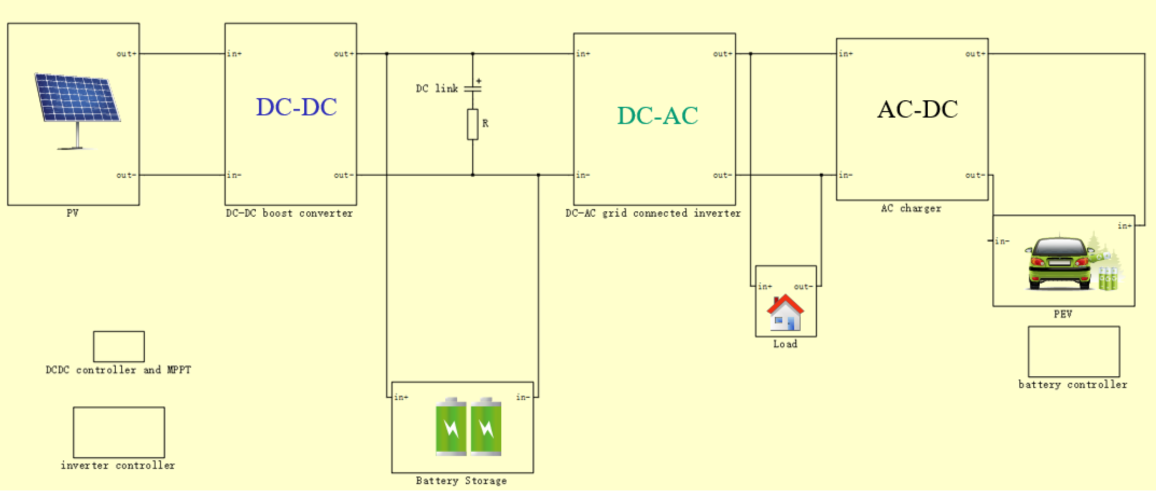

Figure 3. Overall schematic of the proposed system.

From Figure 3, it is noticed that the photovoltaic panel serves as the major renewable energy source. A step-up DC-DC converter is connected to the PV panel for high-efficiency power conversion and achieving the maximum power point tracking of the PV panel. Typically, the voltage of the inverter input should be greater than the maximum value of the inverter output AC voltage to make sure the power generated from the PV can be injected into the grid. The battery storage is connected to the DC link through a bi-directional DC-DC converter. Then, the charging and discharging function can be fulfilled to maintain the power matching. On AC side, the PEV model that represents the load requirements is connected to AC bus. Meanwhile, a simple battery model that is the same as the one on DC side is chosen to demonstrate the PEV battery characteristics. The AC charger is the simple PFC circuits connected with a buck converter. The basic control logic of the whole system is the maximum power point tracking of the PV panel, which is controlled by the DC-DC converter. The DC link voltage and grid current are controlled by the inverter. The coupling point of converter and inverter is a capacitor with enough capacity that is called the DC link [12]. The voltage of the dc link is supposed to be a stable value for the good working condition of the microgrid. Moreover, the DC link capacitor is used to balance the difference between the instantaneous power and the average power of AC side. To make sure all the active power delivered to the grid side, a specific PR (Proportional - Resonant) controller that aims to control the current to be in phase with the grid (Unity power factor) is applied. The control logic (Figure 4) for the inverter side is the cascaded control that the dc link voltage and UPF are controlled only by the inverter.

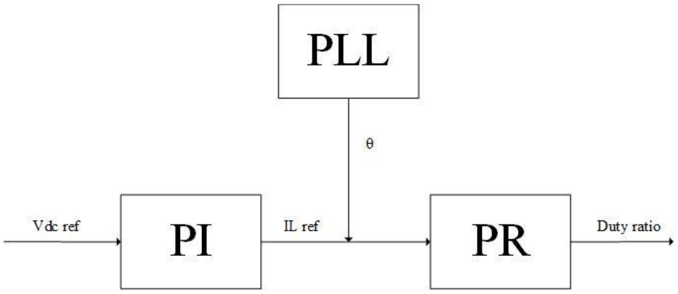

Figure 4.Control diagram of the inverter.

The single-phase string inverter is selected for the modeling procedure, and the basic schematic is shown in Fig.1.

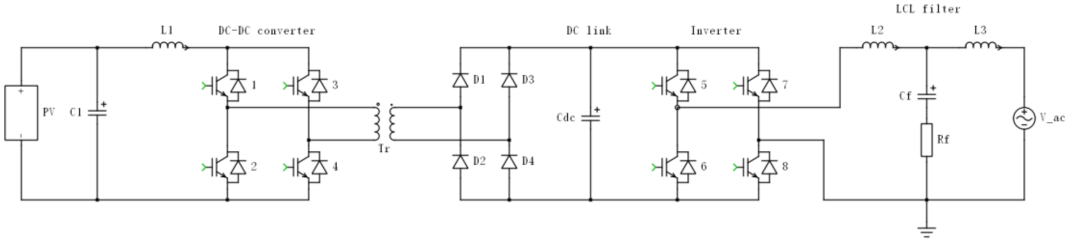

Figure 5.Block diagram of string inverter system.

For DC/DC stage, an isolated boost DC/DC converter is designed for fixed input voltage to meet the requirement of the PV output. In this case, a constant PV output voltage can be achieved through MPPT algorithm. For DC/AC stage, a full bridge unipolar two poles grid-connected inverter is chosen. A fixed DC link voltage control and a grid side current phase control are applied. Once the control goals are achieved, the DC battery storage and the AC side PEV can be connected to the desired area for research purpose.

The MPPT control strategy is based on Incremental conductance MPPT algorithm, which uses the slope of power versus voltage of a PV array to track the maximum power point very rapidly. There are many other MPPT algorithms, and the details are shown in the MPPT controller design section.

To design a specific PV inverter system, a few specifications need to be known (e.g., power rating). The design steps are: first to determine all the inductor, capacitor and other component parameters that can meet the system requirements. Once the plant model is set, designing the controller is the next step. Finally, some simulation plots demonstrate the system response are used to show the overall system behavior.

The specific inverter chosen from the major inverter manufacturer is ABB string inverters PVI-5000-TL-OUTD. The main specifications are shown in Table 1.

Table 1.Specifications of the inverter.

Type code	PVI-5000-OUTD-US
Absolute maximum DC input voltage	600 V
Full power MPPT voltage range	175-530V
Nominal output power	5000W
DC input voltage range	145~530 V
AC voltage range	221~264V
Output frequency range	57-60.5Hz
Total current harmonic distortion	< 2%
Nominal power factor and adjustable range	0.8 inductive to 0.8 capacitive

2.3 PV stage

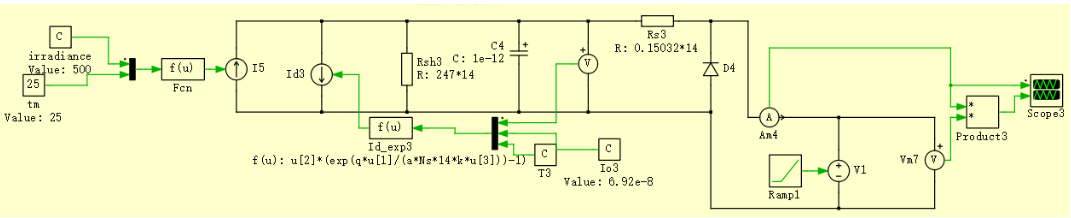

Figure 6. PV panel model in PLECS.

2.3.1 Model derivative

Single diode-based PV cell model is as Figure 7 shows.

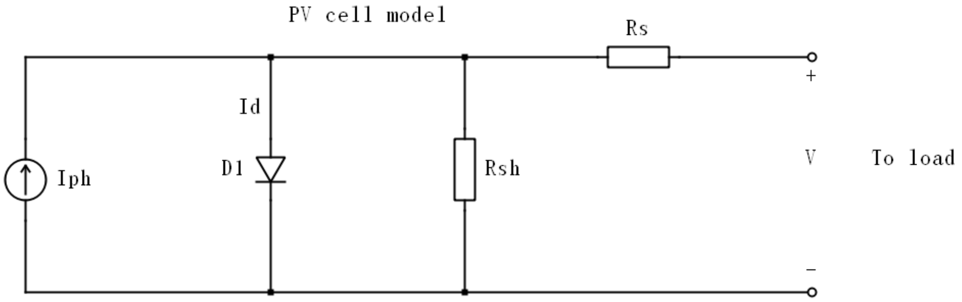

Figure 7. PV cell single diode model.

I_{ph} is the photon current at a specific temperature and irradiance level. Photon current is generated by the internal semiconductors. Ideal PV cell is modeled as a solar-irradiance-dependent current source in parallel with a diode. Since the p-n junction of the inner circuit has unidirectional characteristics, the current in the external circuit is the difference between the photon current and the forward-biased diode current. R_{sh} is called the shunt resistance, which models the leakage current of the p-n junction in the semiconductor. Typically, the R_{sh} value is a large value, with low values representing defective cells. During the low irradiance level, the impact of R_{sh} on the photovoltaic panel efficiency. Meanwhile, the R_s represents the combined resistances of contacts between cells, metal grids, and p and n layers. R_s determines the terminal voltage at which the current begins to drop rapidly as the I-V curve of the PV panel will gradually decrease to zero in a certain voltage. The characteristic equations are listed as follows.

$$I = I_{ph} - I_o\left(e^{\frac{q(V+IR_S)}{akT}} - 1\right) - \left(\frac{V+IR_S}{R_{sh}}\right), \tag{1}$$

$$I_{ph} = (I_{SC_{STC}} + K_1 \Delta T)\frac{G}{G_{STC}}, \tag{2}$$

$$R_{sh} = -\frac{dV}{dI}(at \text{ short circuit}), \tag{3}$$

$$I_o = \frac{I_{sc} - \frac{V_{oc}}{R_{Sh}}}{e^{\frac{V_{oc}}{V_T}}}, \tag{4}$$

$$R_s = -\underset{at \text{ open}}{\frac{dV}{dI}} - \frac{V_T}{I_{sc}}, \tag{5}$$

where I_o is the dark or reverse saturation current of the diode at one temperature. Higher diode quality relates to smaller I_o. I_o increases significantly with temperature. T is temperature, q is the charge of an electron. k represents Boltzman constant, a is diode ideality factor. I_{sc}, V_{oc}, k_1 can be found in the PV cell specification.

The specific PV module is TSM_245_PA0508. So, the model derivation is presented in the following order.

Photon current (at STC),

$$I_{ph} = I_{sc} = 8.68A$$

From the datasheet, zooming in near the short circuit current region at full irradiance (8-9A and 0-10V region)

$$\frac{\mathrm{d}I}{\mathrm{d}V}(at\ SC) = tan\left(-0.53\right) \times \frac{1}{3.153} \times \frac{13.8}{10} = -4.05 \times 10^{-3} A/V$$

$$R_{sh} = 247\Omega$$

Then we calculate the I_0, R_S and a by three nonlinear equations,

$$\frac{\mathrm{d}I}{\mathrm{d}V}(at\ \mathrm{OC}) = -\tan(99.5-90) * \frac{10}{13.8} * \frac{3.15}{1} = -0.382A/V$$

$$R_S = -\frac{\mathrm{d}V}{\mathrm{d}I}(OC) - \frac{V_T}{I_{SC}}$$

$$I_0 = \frac{I_{SC} - \frac{V_{OC}}{R_{sh}}}{e^{\frac{V_{oc}}{V_T}}}$$

$$I_{mp} = I_{sc} - I_0(e^{\frac{V_{\mathrm{mp}} + R_S I_{\mathrm{mp}}}{V_T}} - 1) - \frac{V_{\mathrm{mp}} + R_S I_{\mathrm{mp}}}{R_{Sh}}$$

A simple Matlab code that is shown in appendix is applied to calculate a, R_s and I_0 by sweeping a from 1 to 1.5, then the closest maximum power point at STC can be found.

$$I_0 = 6.91661 * 10^{-8} A, a = 1.304, R_S = 0.15032\Omega$$

2.3.2. Four cases of PV panel plots

P-V and I-V characteristics are shown to demonstrate the dynamics of the PV panel model.

(i) 1000 W/m^2 (STC) for all cells

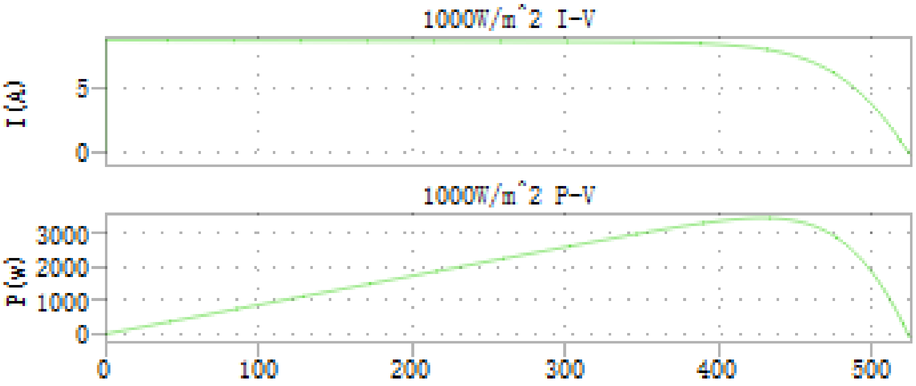

Figure 8. 1000 W/m^2 for all cells characteristic plots.

(ii) 500 W/m^2 for all modules

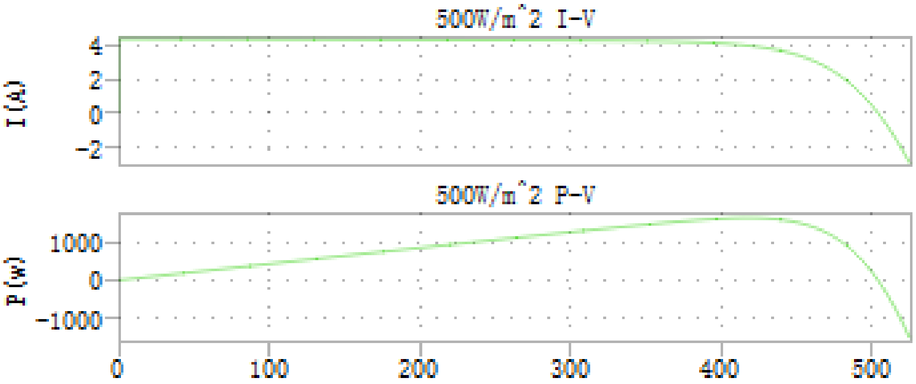

Figure 9. 500 W/m^2 for all modules characteristic plots.

(iii) 200 W/m2 for all modules

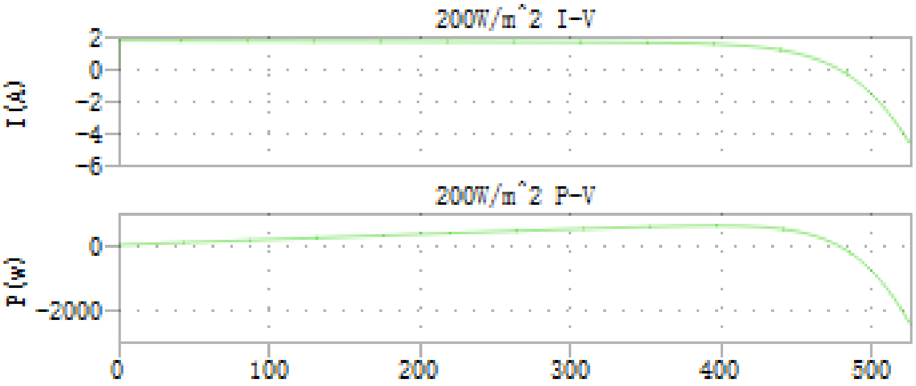

Figure 10. 200 W/m^2 for all modules characteristic plots.

(iv) 500 W/m2 for 1/3rd of the total number of cells, 800 W/m2 another 1/3rd of the total number of cells, and 1000W/m2 for the remaining cells.

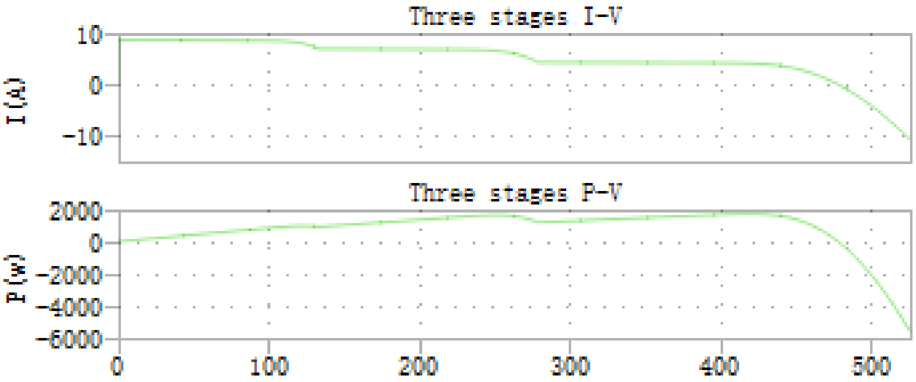

Figure 11. Three stages for all modules characteristic plots.

2.4 DC-DC Converter Design

The DC-DC converter has a wide range of categories: buck converter, boost converter, buck-boost converter, flyback converter, etc. Different converters have different topologies. Suitable topologies are chosen according to different system requirements. For this DC-DC stage, the isolated boost DC-DC converter is chosen for its galvanic isolation capacity, compared with the non-isolated DC-DC converter. For designing a scaled-down DC-DC converter with a low voltage rating, the non-isolated DC-DC converter is suitable since the new standard of IEEE does not require an isolated transformer. The isolated DC-DC converter is much more suitable for a high power PV inverter. Another characteristic is that in PV inverter system, there is no need for boost converter to be bidirectional, because this PV application needs no power from AC grid. The topology of the isolated-boost DC-DC converter is shown below.

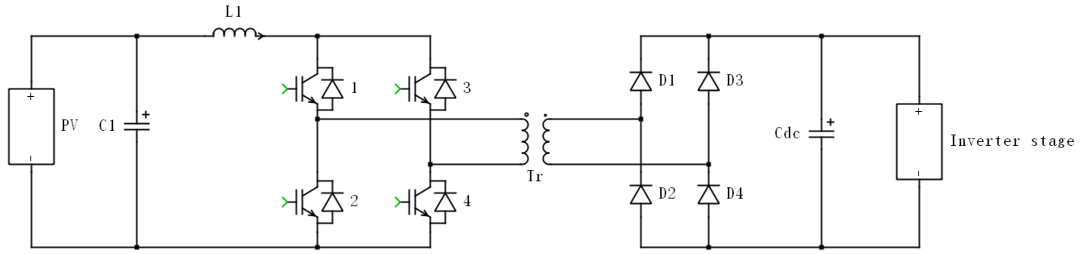

Figure 12. Isolated-boost DC-DC converter schematic.

The input of this converter is the PV string output that has a wide range of voltage variations due to different irradiances and temperatures or panel characteristics. The output of which is typically 400V or higher constant value (with 120Hz ripple) that accommodates different grid voltages (typical 240V). The control goal of the duty ratio is defined to track the maximum power of the PV panel.

The relationship between input voltage and the output voltage is as follows.

$$V_{in} = \frac{(1-D)}{n} V_o \quad . \tag{6}$$

So, the turns-ratio of the transformer is calculated below.

$$n = \frac{V_o(1-d_{\min})}{V_{in\max}} \quad . \tag{7}$$

Choosing d_{min}=0.1,

$$n = \frac{V_o(1-d_{\min})}{V_{in\max}} = \frac{400(1-0.1)}{524} = 0.69$$

Design L: to limit inductor current ripple ΔI_L to 5% of maximum average inductor current (Typically the ripple is 3-5% maximum value of the current, which should be selected).

$$\Delta I_L = 0.05 * \frac{5000}{145} = 1.72A$$

$$L_{in} = \frac{\frac{V_o}{n} D(1-D)\frac{T_s}{2}}{\Delta I_L} = \frac{\frac{400}{0.69} * 0.5 * 0.5 * 25 * 10^{-6}}{1.72} = 2.1mH$$

It is better to choose a relatively higher value for making the system response more reasonable and ideal, L=5mH.

Design of C: The output capacitor, which is connected to DC/AC stage will induce 120Hz voltage ripple. The selected capacitor should limit this voltage ripple lower than 10% of average dc-link voltage. The dc-link capacitor can be calculated below.

$$C_{dclink} = \frac{2P_o}{4V_o \omega (0.5 \Delta V_o)} = \frac{2 * 5000}{4 * 400 * 377 * 0.5 * 40} = 830 \mu F$$

Finally, the capacitance of the dc-link capacitor can be selected as $3mF$

The input capacitor is used to limit the voltage ripple induced by inductor current ripple, which can be calculated as below,

$$C_{in} = \frac{\Delta I_L}{\Delta V_{in}} * \frac{1}{8 f_s} = \frac{1.72}{58} * \frac{1}{8 * 50 * 10^3 * 2} = 3.71 * 10^{-8} F$$

Finally, to get smaller voltage ripple, a larger capacitor should be chosen, the selected value is $10 \mu F$.

The specifications of the DC-DC stage are shown in the Table 2.

Table 2. Specifications of the DC-DC stage.

Type code	Value
DC Input voltage	524V
DC Output voltage	400V
Maximum Output power	5000W
Frequency switching rate	50kHz
Duty Cycle(min)	0.1
Transformer turn ratio	0.69
L_{in}	5mH
C_{dclink}	3mF
C_{in}	10uF

The DC/DC isolated boost converter is shown in the following figure.

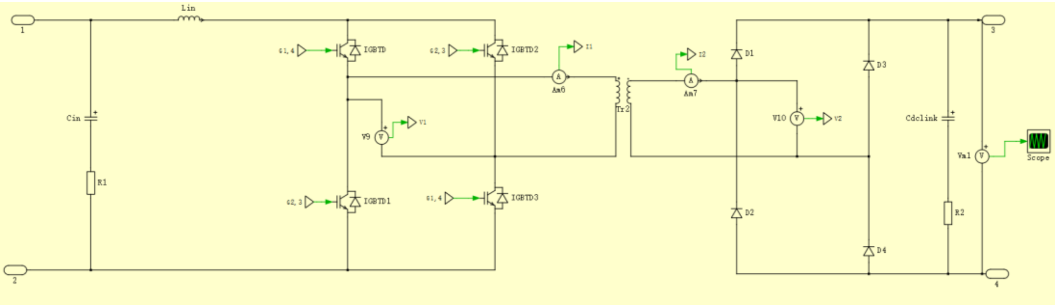

Figure 13. Schematic of DC/DC boost converter.

The bidirectional DC-DC converter design procedure for DC battery charger is the same as this section listed above. The inductor value and capacitor value should be within the system requirements. The simple PI controller is also designed for regulating the output of the converter to charge the battery.

2.5 DC-AC inverter design

Full bridge inverter is commonly used in DC-AC transformation, and this popular topology is chosen for its low cost and low loss. There are also many other topologies designed for some specific cases. PV inverter system usually chooses the full bridge inverter controlled by unipolar PWM wave. The unipolar switched inverter offers reduced switching losses and generates less EMI compared to bipolar PWM controlled inverter.

According to the specifications of the DC-AC inverter, the output current THD should be lower than 2%. The switching frequency is 20kHz, the maximum line current is 23A RMS. The equation for calculating THD is shown below.

$$THD = \frac{\Delta I_{RMS}}{I_{g.linecurrnt}}, \tag{8}$$

$$\Delta I_{RMS} = \frac{T_S V_d}{L\sqrt{12\pi}} m_a \sqrt{\frac{3\pi}{8} m_a^2 - \frac{8}{3} m_a + \frac{\pi}{2}}, \tag{9}$$

The ΔI_{RMS} should less than $23*2\% = 0.46A$ RMS. Thus, the inductance of output filter can be calculated,

$$L = \frac{T_S V_d}{\Delta I_{RMS}\sqrt{12\pi}} m_a \sqrt{\frac{3\pi}{8} m_a^2 - \frac{8}{3} m_a + \frac{\pi}{2}}. \tag{10}$$

The calculation process is by substituting $m_a = \frac{221*1.414}{400} = 0.781$. Thus, L=1.3mH. The final value of the inductor can be selected as 3mH for better system performance.

The DC/AC inverter schematic is as follows.

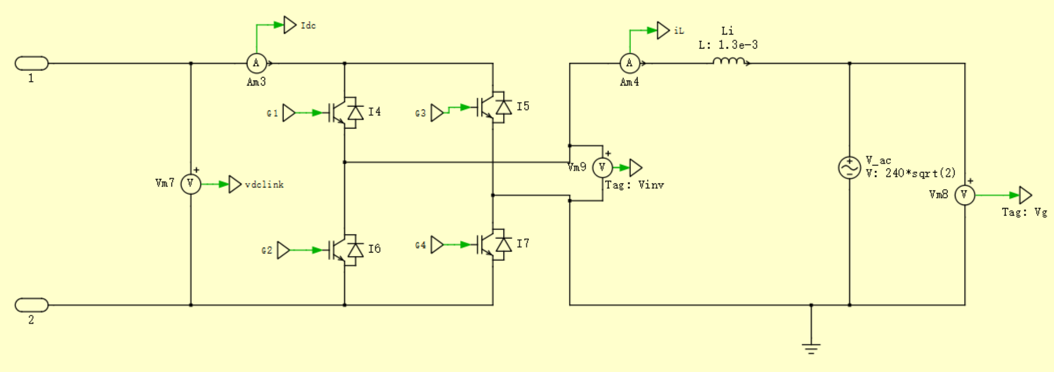

Figure 14. Schematic of DC/AC inverter connected to the grid.

For AC side PEV charger design, the most popular topology for PFC circuit is single phase boost PFC, which is the AC-DC rectifier, and the schematic is the full bridge diode connected with a boost converter. Moreover, the controller design is the same as the inverter, which will be demonstrated in the next section. The output voltage is regulated to a constant value. Meanwhile, the output current should be controlled to follow the rectified voltage.

2.6. Controller design of the whole system

2.6.1 DC/AC control

The inverter output current control is applied to control the current through the filter in phase with the utility grid, which is to make sure all the power delivered from the PV panel is consumed by the load. In another way, the unity power factor is achieved. The main functions of the DC-AC inverter can be summarized as generating AC output current in phase with the AC utility grid voltage and balancing power between PV and Grid. Meanwhile, providing a constant dc link voltage that can be utilized as an energy storage site. Last, the inverter should maintain high power conversion efficiency and high reliability, also low switching loss. A block diagram is shown to demonstrate the control logic.

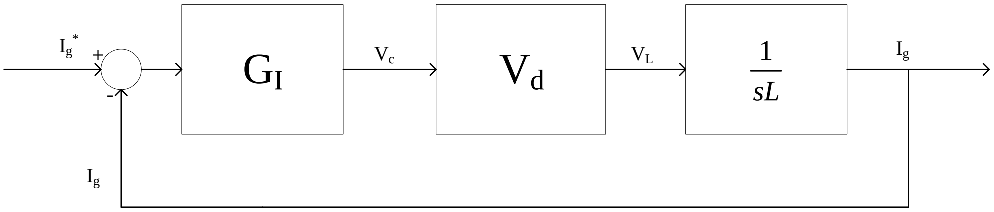

Figure 15. Current control diagram.

The single filter is applied to connect the inverter to the grid, which reduces the harmonics of the inverter output current. The first choice of the current controller is PI controller, which will lead to result in a large steady-state error in current. Grid voltage feedforward is used to reduce the error. Besides, Proportional-resonant (PR) controller significantly can reduce the steady-state magnitude and phase errors without requiring grid voltage feedforward. Since the gain at 60Hz is very large. in this thesis, the PR controller is chosen for its better performance. The transfer function is given below.

$$G_{PR}(s) = K_p + K_I \frac{s}{s^2+\omega^2}, \tag{11}$$

The bandwidth is chosen as 2 kHz, and phase margin is 60°. The transfer function of the plant is given below.

$$G_{PL}(s) = \frac{V_d}{Ls} = \frac{400}{1.5*10^{-3}s}$$

$$K_P = \frac{1}{|G_{PL}(j\omega_c)|} = \frac{1}{|G_{PL}(j4000\pi)|} = 0.0471$$

$$K_I = (\frac{1000}{G_{PL}(j*\omega_l)} - K_P)*\left|\frac{(j\omega_l)^2+\omega_r^2}{j\omega_l}\right| = 11.95$$

where, $\omega_l = 2\pi * 59.3 rad/s,\ \omega_r = 2\pi * 60 rad/s \quad \omega_c = 4000\pi$

Thus, the PR controller transfer function is shown as below.

$$G_c = 0.0471 + 11.95 * \frac{s}{s^2 + (2\pi * 60)^2}$$

Next part is about the outer loop DC link voltage controller design, which is regulated by a feedback controller, the block diagram is shown below.

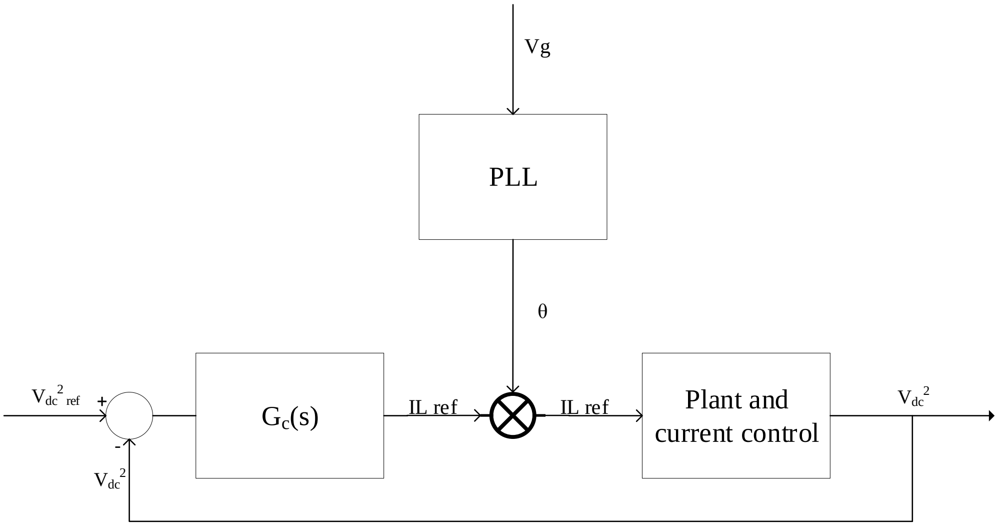

Figure 16. DC link voltage control diagram.

The current loop controller has been designed before, the transfer function of the plant is calculated.

$$G_p = \frac{V_{DClink}^2(s)}{\hat{I}_{Li}(s)} = \frac{-\hat{V}_g}{sC_{DClink}}, \tag{12}$$

To make the design procedure easier, the reverse of the equation above is adopted to design the controller.

$$G_p^{'} = \frac{V_{DClink}^2(s)}{\hat{I}_{Li}(s)} = \frac{\hat{V}_g}{sC_{DClink}}, \tag{13}$$

So, this plant is shown below.

$$G_p^{'} = \frac{240*\sqrt{2}}{s*3*10^{-3}}$$

The k-factor method is applied to design the controller, The cross-over frequency is chosen to be 15Hz, and the phase margin is 60^o.

$$\begin{aligned}
&phi\_sys = \arg(G_p(j\omega_c)) = -90^o \\
&phi\_boost = (60-90) - phi\_sys = 60^o \\
&k = \tan(\frac{phi\_boost}{4} + \frac{\pi}{4}) = 3.732 \\
&\omega_z = \frac{\omega_c}{k} = \frac{30\pi}{3.732} = 25.254 rad/s \\
&\omega_p = \omega_c * k = 351.738 rad/s \\
&K_c = \frac{1}{\left| G_p(j\omega_c) * \frac{1}{j\omega_c} * \frac{1+j\frac{\omega_c}{\omega_z}}{1+j\frac{\omega_c}{\omega_p}} \right|} = 0.021
\end{aligned}$$

Finally, the transfer function of the DC link controller is shown as below.

$$G_c(s) = \frac{0.021}{s}\left(\frac{1+\frac{s}{25.254}}{1+\frac{s}{351.733}}\right)$$

2.6.2. PLL controller design

Next step is to design a suitable PLL (phase locked loop) controller for grid synchronization, which is used to make the inverter output be in phase with the grid voltage. The Phase-locked loop (PLL) is the predominant technique for grid synchronization of PV inverter. Any errors of synchronization will lead to an uncontrolled exchange of energy between the inverter and grid, which results in highly oscillations and overcurrent and voltage, even damaging the switching device. PLL controller first compares the input and output waveforms to generate a voltage proportional to the phase difference. But there is also twice the ac frequency component in it. Then a low pass filter is applied to get rid of this high-frequency component. Finally, the voltage-controlled oscillator generates the sine and cosine wave with frequency and phase information according to the input voltage. The block diagram of the PLL controller system is shown as follows.

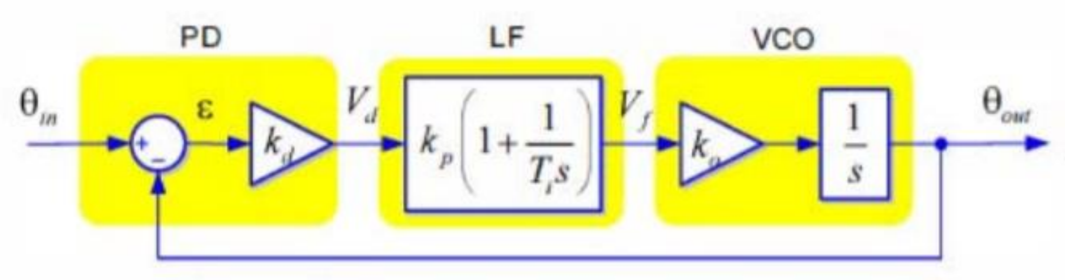

Figure 17. Phase lock loop control diagram [41].

The plant transfer function is shown as below.

$$G_p(s) = \frac{1}{s}. \tag{14}$$

The k-factor method is also applied to design the PLL controller. $\omega_c = 2\pi * 6$, and the phase margin is 60°.

$$G_p(s) = \frac{1}{s}$$

$$phi\_sys = \arg(G_p(j\omega_c)) = -90^o$$

$$phi\_boost = (60-90) - phi\_sys = 60^o$$

$$k = \tan(\frac{phi\_boost}{4} + \frac{\pi}{4}) = 3.732$$

$$\omega_z = \frac{\omega_c}{k} = \frac{12\pi}{3.732} = 10.101 rad/s$$

$$\omega_p = \omega_c * k = 140.695 rad/s$$

$$K_c = \frac{1}{\left| G_p(j\omega_c) * \frac{1}{j\omega_c} * \frac{1+j\frac{\omega_c}{\omega_z}}{1+j\frac{\omega_c}{\omega_p}} \right|} = 380.816$$

Finally, the transfer function of the controller is derived.

$$G_c(s) = \frac{380.816}{s}\left(\frac{1+\frac{s}{10.101}}{1+\frac{s}{140.695}}\right)$$

The following Table 3. shows the specifications for DC/AC inverter power stage.

Table 3. Specifications for DC/AC stage.

DC input voltage	400V
Grid voltage(RMS)	240V
Maximum output power	5000W
Switching frequency	20kHz
Filter inductor	3mH

The overall DC/AC inverter side control block is implemented.

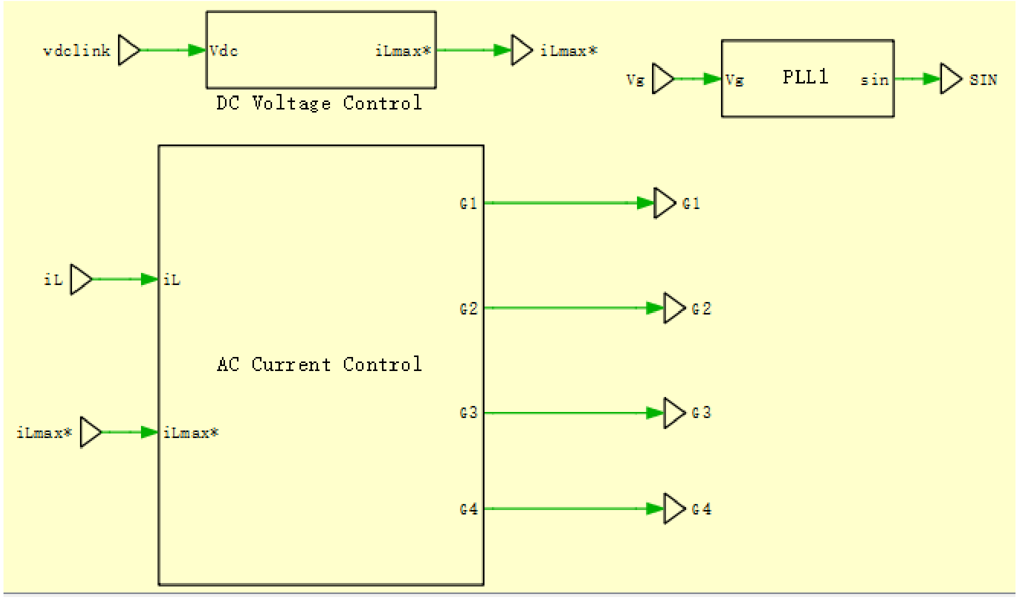

Figure 18. Schematic of whole control diagram.

2.6.3. DC-DC controller design

The major task for the DC-DC controller is to guarantee the PV panel working at the maximum power point according to the requirement of the system. The DC-DC step-up converter converts the relatively low voltage to a higher level for reducing the power loss. Due to the reason that most of the power loss comes from the RMS current, with high voltage in a fixed power situation, the current will be relatively low. Thus the power loss will become small.

To design the voltage controller, the isolated boost converter can be regarded as a buck converter. The voltage controller can also be designed according to the k-factor method. The bandwidth is selected as 2000Hz. PM equals to 60^o. The detailed design steps are as follows.

$$G_p(s)=\frac{\frac{V_{dc}}{n}(1+ESR*C_{in}*s)}{L_{dc}*C_{in}(1+\frac{ESR}{R_L})s^2+(ESR*C_{in}+\frac{L_{dc}}{R_L}s+1)}=\frac{\frac{400}{0.69}(1+0.01*10*10^{-6}s)}{5*10^{-3}*10*10^{-6}*(1+\frac{0.01}{40})s^2+(0.01*10*10^{-6}+\frac{5*10^{-3}}{40})s+1}$$

$$phi\_sys=\arg(G_p(j\omega_c))=-167.18^o$$

$$phi\_boost=(45+167.18)-90=122.18^o$$

$$k=\tan(\frac{phi\_boost}{4}+\frac{\pi}{4})=3.879$$

$$\omega_z=\frac{\omega_c}{k}=\frac{4000\pi}{3.879}=3238rad/s$$

$$\omega_p=\omega_c*k=48720rad/s$$

$$K_c=\frac{1}{\left|G_p(j\omega_c)*\frac{1}{j\omega_c}*\frac{1+j\frac{\omega_c}{\omega_z}}{1+j\frac{\omega_c}{\omega_p}}\right|}=10.183$$

Then, the transfer function of voltage controller can be expressed as follow:

$$G_c(s) = \frac{10.183}{s} \frac{(1+\frac{s}{3238})^2}{(1+\frac{s}{48720})^2}$$

2.6.4. MPPT control design

There are many MPPT algorithms for PV panel, such as PnO, incremental inductance, climb hills, etc. Different methods have their pros and cons. In this thesis, the incremental inductance method is implemented to control the PV panel to work at the maximum power point.

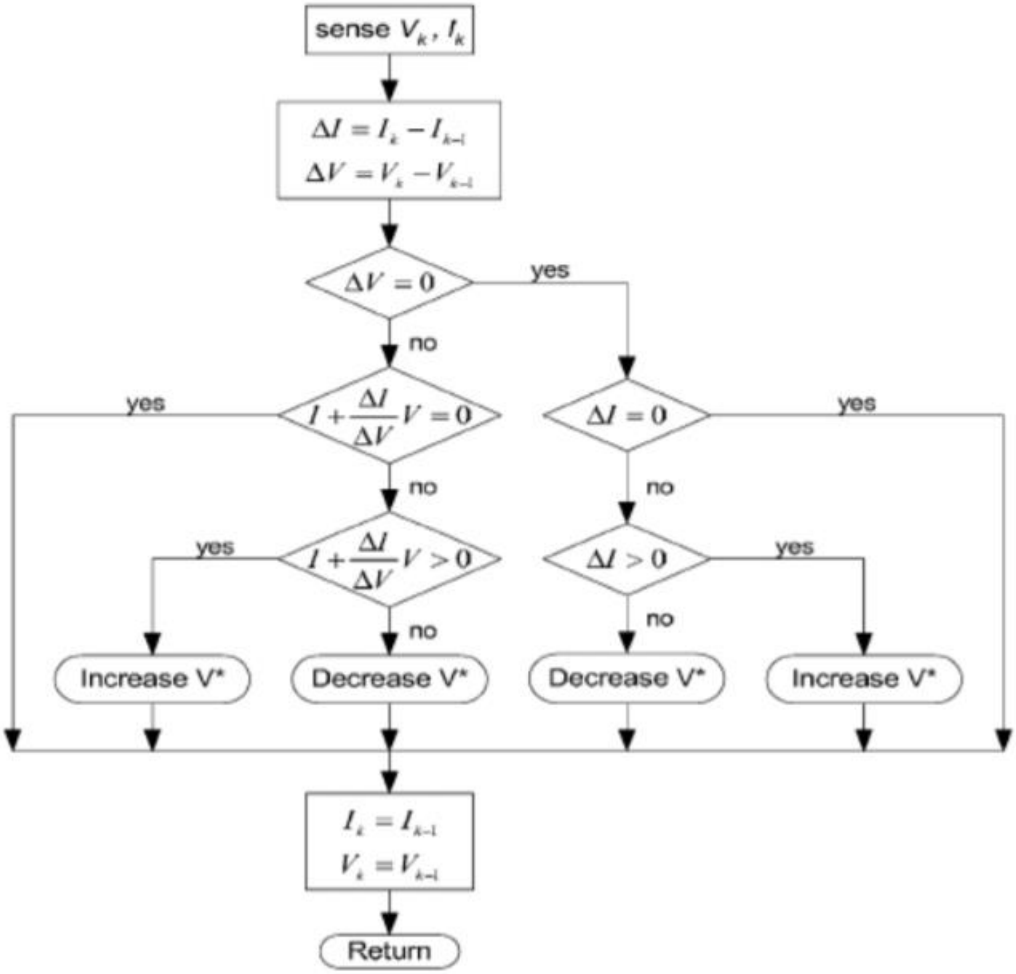

Figure 19. Incremental conductance MPPT algorithm flowchart [40].

The flow chart shown above is the Incremental conductance MPPT algorithm. The control index is determined by the differential of PV power (dP) and PV voltage (dV). The total control of DC/DC stage is shown as below.

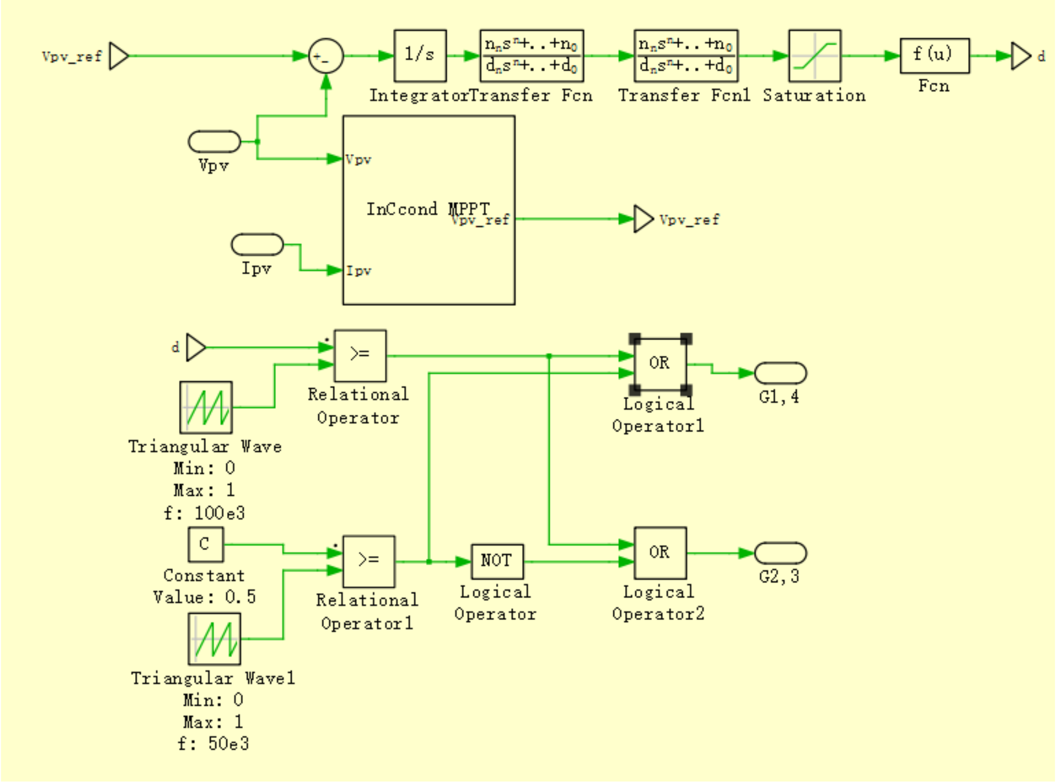

Figure 20. Schematic of MPPT implementation.

2.6.5. Simulation results and system performance analysis

Condition : 1000W/m2, 50°C

Plots1: PV array output voltage and current, output power**.**

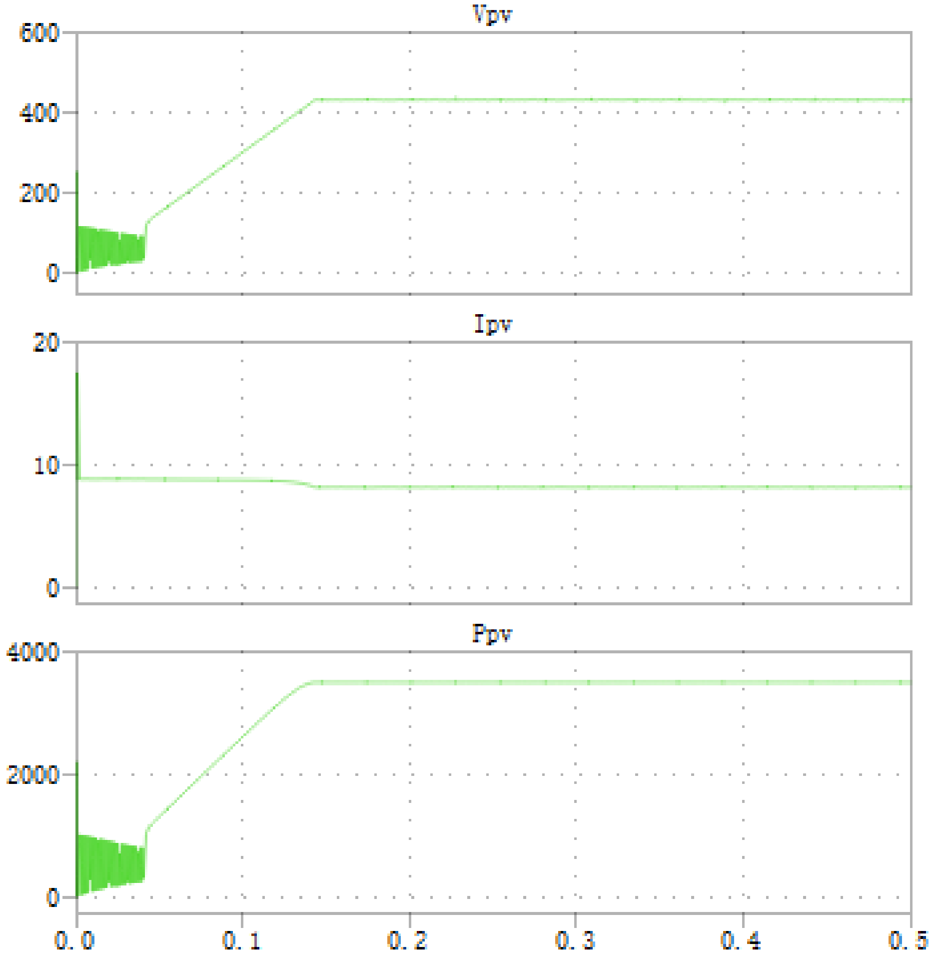

Figure 21. PV array output voltage and current, output power.

Plots2: Transformer voltage and current (V1, I1 are the primary voltage and current, V2, I2 are the secondary voltage and current)**.**

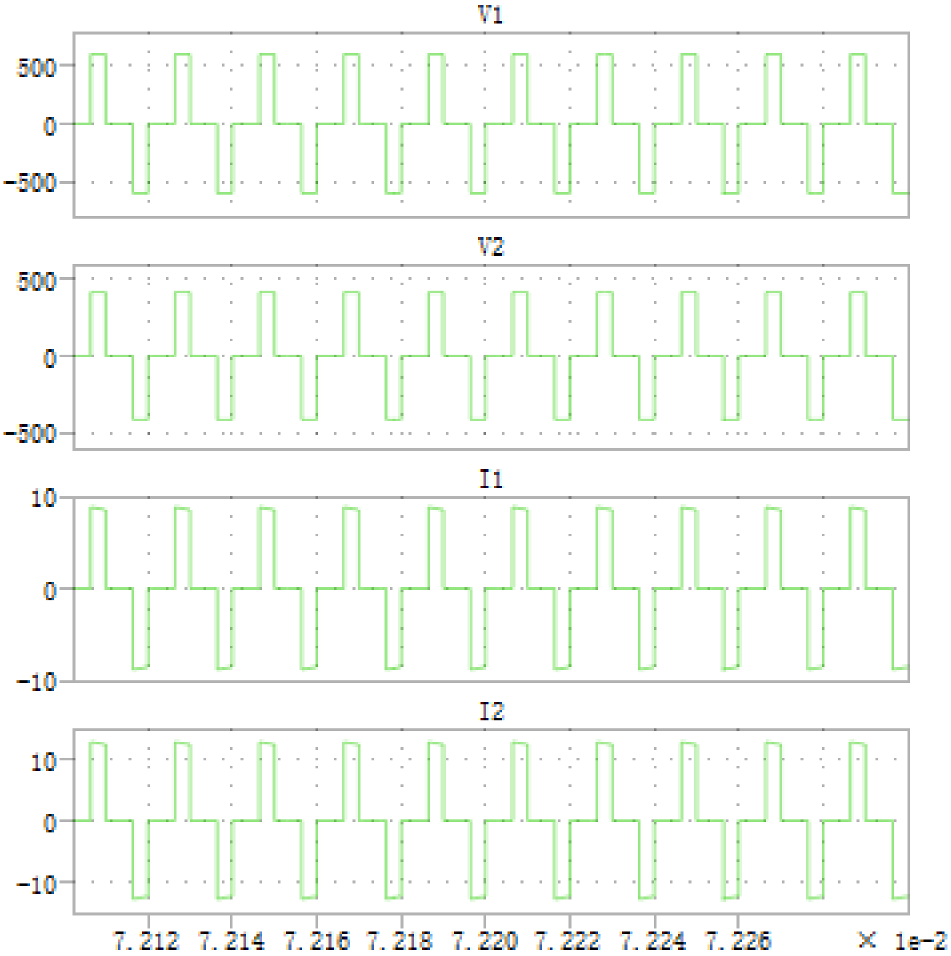

Figure 22. Transformer voltage and current.

Plots 3: Inductor voltage of DC-DC stage.

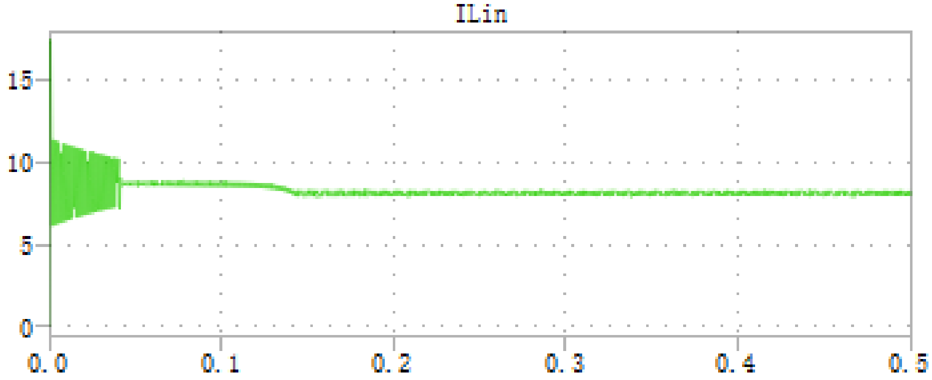

Figure 23. Inductor voltage of DC-DC stage.

Plots 4: PWM voltage.

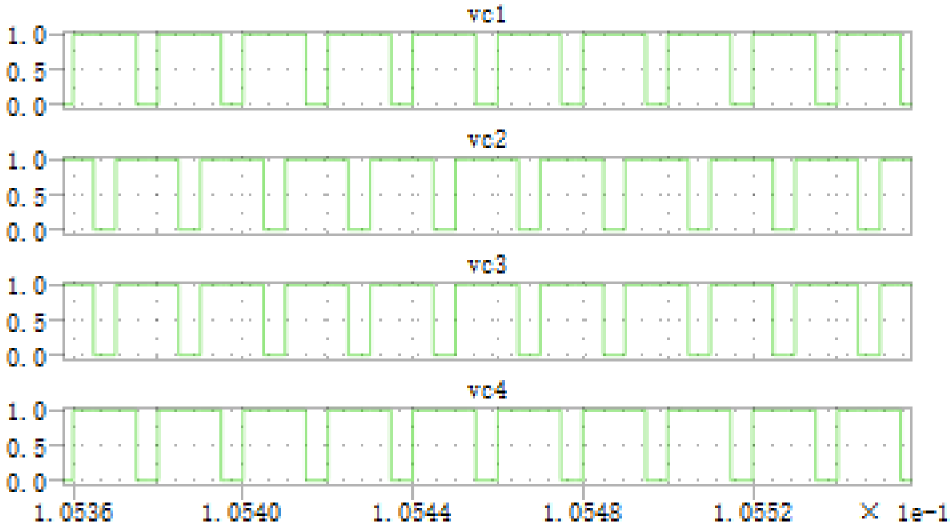

Figure 24. PWM voltage.

Plots 5 Grid current.

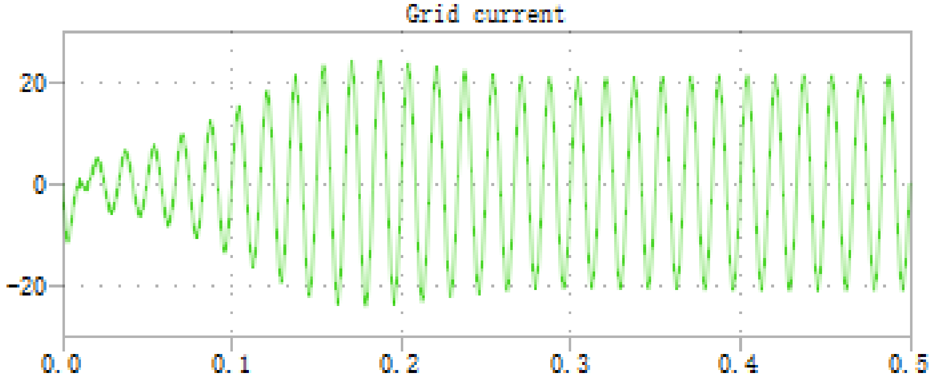

Figure 25. Grid current.

Plots 6 Switching and average values of DC link current.

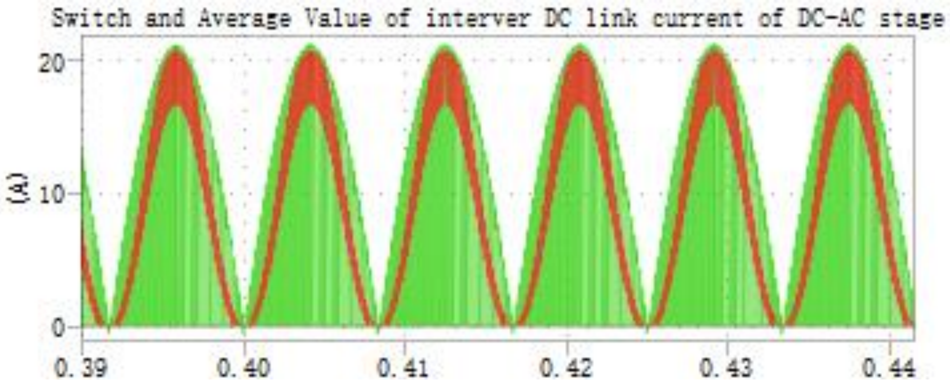

Figure 26. Switching and average values of DC link current.

For demonstrating the peak-peak ripple in the DC side inductor current matches with the calculation analysis, first, the inductor current detailed plot is presented.

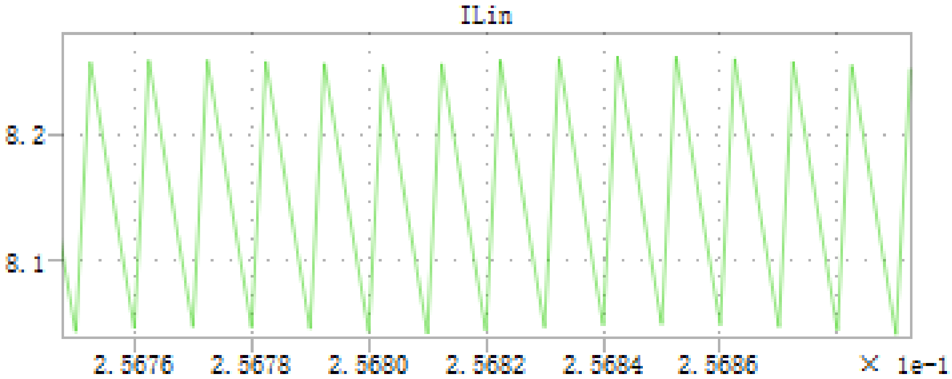

Figure 27. Detailed ILin current.

As seen in the figure, the ripple is around 0.2A, which is because the calculated inductor value is 2.1mH, the real value used for simulation is 5mH. The calculated pk-pk ripple value is 1.72A. The simulation result is within the range value. So, this is a valid simulation.

For DC link voltage ripple, a specific graph is also shown below.

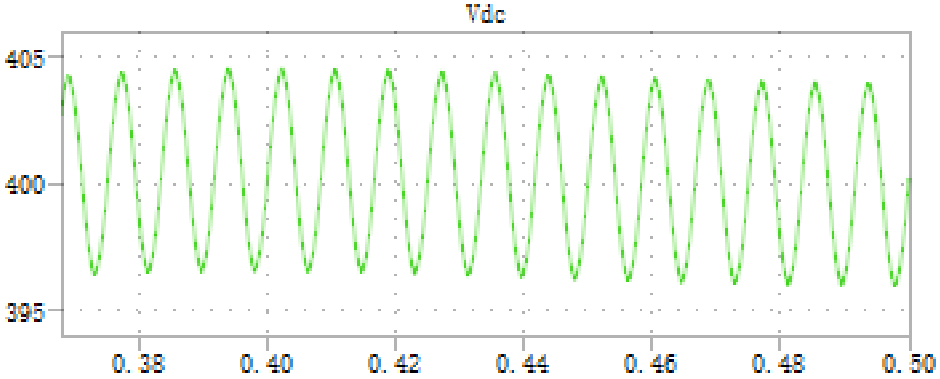

Figure 28. Detailed V_{dc}.

As is shown in the figure, the voltage ripple is around 8V. the maximum ripple value is around 40V, the calculated value is 830e-6F. But the real value used is 3e-3F to make the plot more precise. The simulation result is within the maximum value, which demonstrated the value match with the analytical calculations.

THD of the grid side line current: From THD analysis in PLECS, the THD of grid current is 0.0183975, which is within 2% of the specification.

3. SIMPLIFIED MATHEMATICAL PV MICROGRID MODEL

3.1 Mathematical model of the PV microgrid in Simulink

For the mathematical model of the microgrid, the model is as the following figure shows.

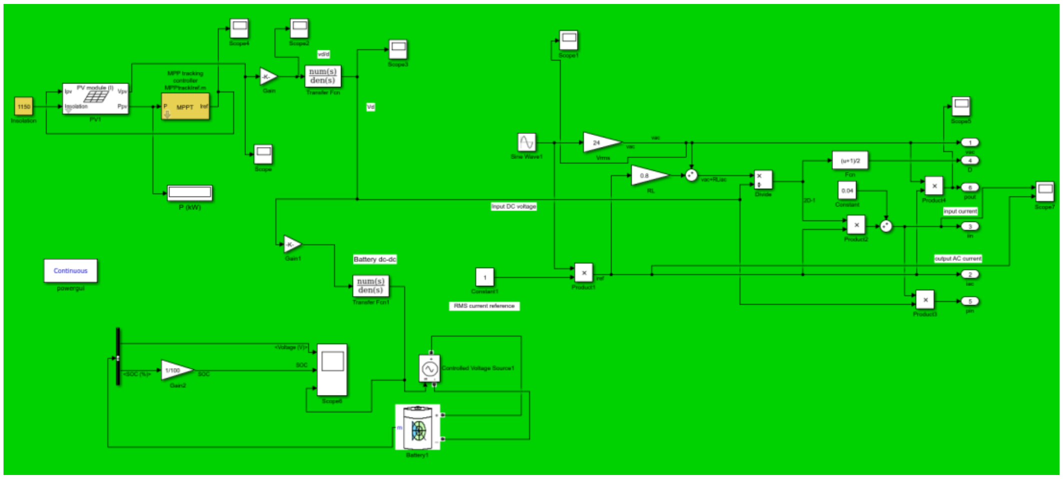

Figure 29. Complete average mathematical model.

The model is based on a purely mathematical model, which can be used for energy allocation analysis. This PV model has MPPT algorithm combined in it. The output of this MPPT module is Iref, which is the input of the PV module. It is a little bit different from the Plecs control logic. In PLECS software, the control logic is basically using MPPT algorithm to generate V_{ref}, and then the reference is compared with real-time V_{pv}. The error generated is going through the controller, the output of which is the duty ratio d. Next, the duty ratio is compared with a triangular wave to get PWM wave that used as the switch signal of the switch (e.g., MOSFET) in DC-DC converter. Hence, with the control of DC-DC converter, the PV panel can work at the maximum power point.

3.1.1 PV panel

From the left-hand side, a PV module with MPPT algorithm is presented, the environmental influence on the PV module is only the irradiance level, the temperature is not considered.

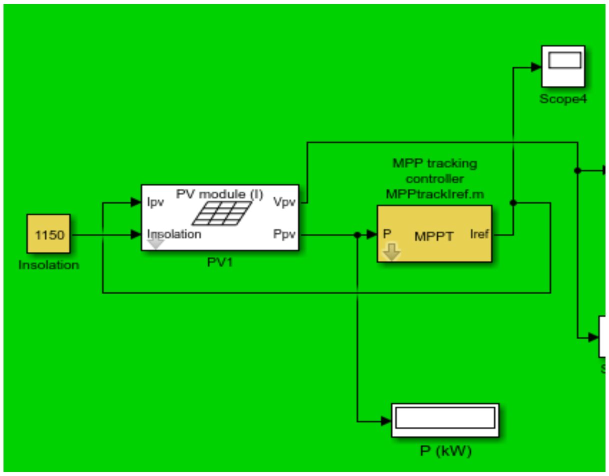

Figure 30. PV model block.

Then an algebraic constraint block is adapted to calculate the corresponding single PV cell voltage. And the MPPT algorithm is simply PnO method that is the most commonly used MPPT algorithm. The basic idea of this method is the voltage varies under the influence of a small perturbation, and the corresponding power is compared with the power in the previous perturbation period. When the power is going up, the voltage should be increased, on the contrary, the perturbation reverses.

3.1.2 DC-DC converter

Next part is the DC-DC boost converter. Basically, the schematic is a transfer function, which is V_{bus} divided by duty ratio. The duty ratio is a constant value, since a desired value of V_{bus} is known, and the V_{pv} is also fixed by the MPPT algorithm, the ratio of these two values is the duty ratio that is also the input of the transfer function. Below is the converter diagram representation.

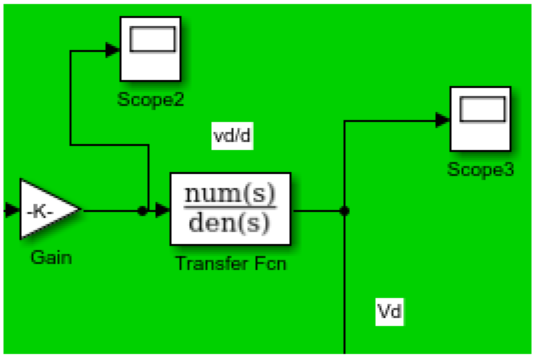

Figure 31. DC-DC boost converter block.

The transfer function is shown as below.

$$\frac{\tilde{v}_o}{d}=\frac{V_o}{1-D}\frac{(1-\frac{sL_e}{R_L})(1+sCR_{ESR})}{1+s[\frac{L_e}{R_L}+CR_{ESR}]+s^2L_eC(1+\frac{R_{ESR}}{R_L})}\ , \qquad (15)$$

$$L_e=\frac{L}{(1-D)^2}$$

where R_L value can be determined by the power matching. P_{in} equals to P_{out}. d is the duty ratio of the converter, R, L and C are the corresponding values in the converter. For the DC-DC converter used to charge the battery, it is the transfer function of buck converter that is similar to boost converter.

3.1.3 Inverter schematic

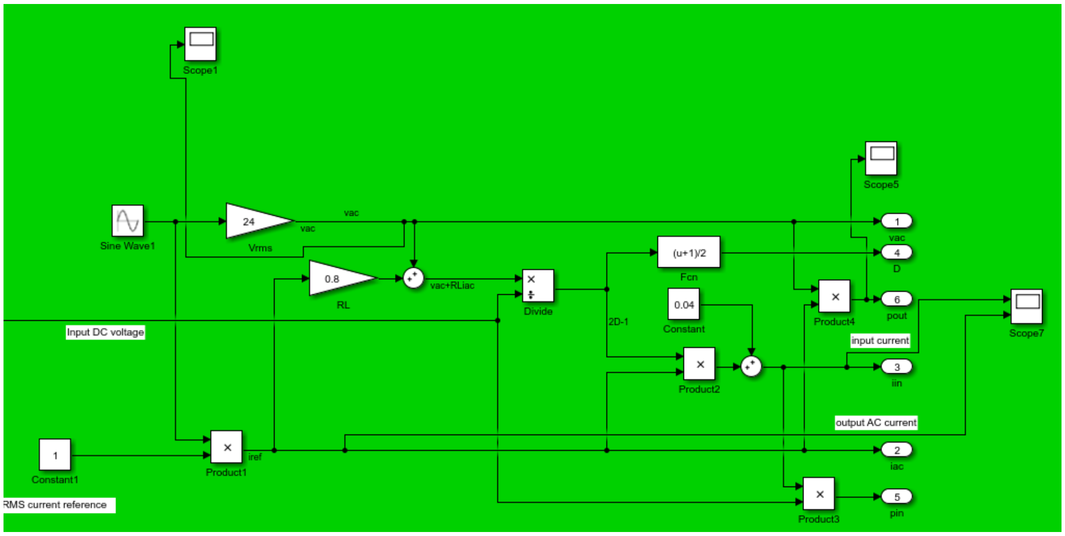

Figure 32. Single phase inverter block.

The fundamental math equations for the inverter are presented below.

$$P_{in} - P_{loss} = P_{out}$$

$$\frac{V_{ac} + R_L * I_{ac}}{Vbus} = 2D - 1, \qquad (16)$$

where Pin is the input power of the inverter, Ploss is the switching loss in the inverter, Pout is the inverter output power. D denotes the duty ratio, RL is the line resistance, The sine wave multiplied by a gain value represents the output value of inverter.

The battery charger model in this mathematical model is the same as the transfer function as the buck converter, which demonstrates the charging situation. The battery model is the standard lithium-ion battery model.

4. STATE SPACE MODEL OF DIFFERENCE POWER STAGES OF PV INVERTER MICROGRID

4.1 DC-DC boost converter

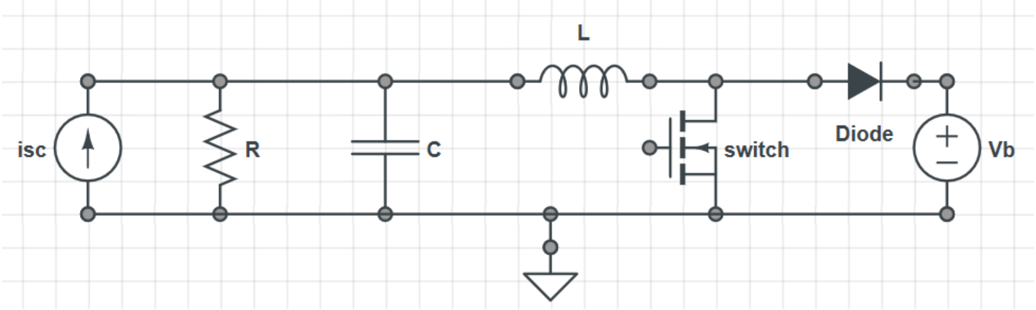

Figure 33. DC-DC converter schematic.

$$\begin{aligned}\frac{\partial i_L}{\partial t} &= \frac{V_c}{L} - \frac{V_b(1-d)}{L} \\ \frac{\partial V_c}{\partial t} &= \frac{i_{sc}}{C} - \frac{V_c}{C*R} - \frac{i_L}{C}\end{aligned}, \tag{17}$$

for this model, Current source paralleled with resistor and capacitor is the average model of PV panel. The middle part that contains inductor, diode, and the switch is the DC-DC converter model. d equals to the switching ratio.

In this case, V_c in the equation can be regarded as the output from PV panel, V_b can be regarded as the voltage of DC bus, which is regulated by the inverter. By applying the basic KCL and KVL to inductor and capacitor, the dynamics equation of the inductor and capacitor are shown in the equations above respectively.

4.2 DC-AC Grid-connected inverter with LCL filter model

For Grid connected inverter side, the basic schematic is shown in the below picture:

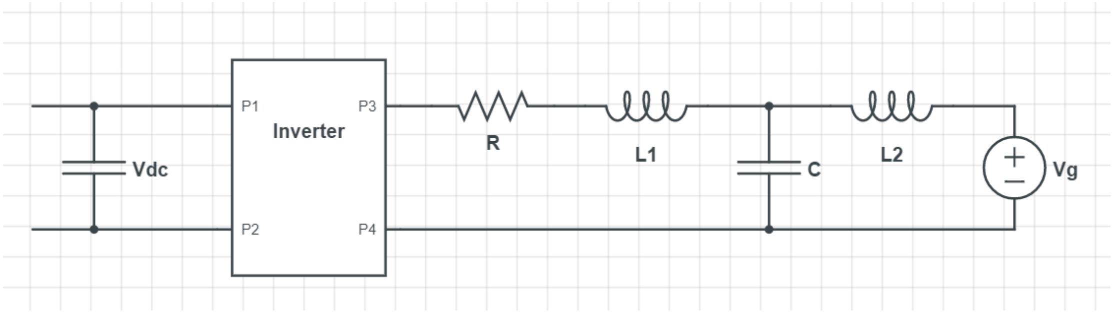

Figure 34. Grid-connected inverter with DC link.

Generally, the AC side is the inverter connected to the grid through LCL filter, which is used to get rid of the harmonics generated by inverter high-frequency switch cycle. Using KCL and KVL law, the state equations can be derived.

$$\begin{aligned} L_1 \frac{\partial i_1}{\partial t} &= V - (i_1 * R + V_c) \\ L_2 \frac{\partial i_2}{\partial t} &= V_c - V_g \\ C \frac{\partial V_c}{\partial t} &= i_1 - i_2 \end{aligned} \quad . \tag{18}$$

Then, the state space equations are as follows.

$$\begin{bmatrix} \frac{\partial i_1}{\partial t} \\ \frac{\partial i_2}{\partial t} \\ \frac{\partial i_3}{\partial t} \end{bmatrix} = \begin{bmatrix} -\frac{R}{L_1} & 0 & -\frac{1}{L_1} \\ 0 & 0 & \frac{1}{L_2} \\ \frac{1}{C} & -\frac{1}{C} & 0 \end{bmatrix} \begin{bmatrix} i_1 \\ i_2 \\ i_3 \end{bmatrix} + \begin{bmatrix} \frac{1}{L_1} & 0 \\ 0 & -\frac{1}{L_2} \\ 0 & 0 \end{bmatrix} \begin{bmatrix} V \\ V_g \end{bmatrix},$$

where i_1, i_2 are the currents going through inductor L_1, L_2 respectively, V is the voltage cross Port3 and Port4, which is the inverter output voltage, V_c denotes the capacitor voltage, V_g and V_{dc} are grid voltage and dclink voltage.

4.3 Bi-directional DC-DC converter model

For battery connected to the DC bus, state space model [34] is illustrated as follows, Bi-directional DC-DC converter using a current generator, it is considered that the high voltage side of the converter as dependent current source, since it is controlled by inverter side, Vlow is the battery voltage.

Switch S1, S2 control the flow directions (Charging and discharging).

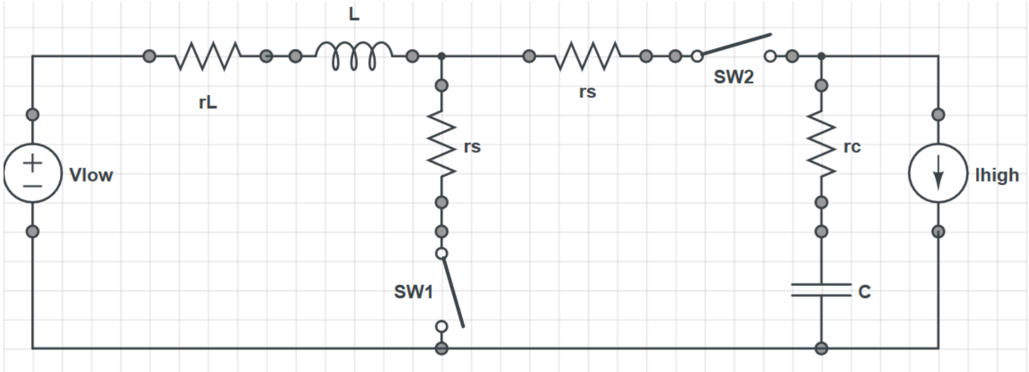

Figure 35. Bi-directional DC-DC converter circuits.

SW2 on:
$$C\frac{\partial V_c}{\partial t} = D^{'}(i_L - I_{high})$$
$$L\frac{\partial i_L}{\partial t} = D^{'}(V_{low} - V_c - rc(iL - I_{high}) - i_L(rL + rs))$$

SW1 on:
$$C\frac{\partial V_c}{\partial t} = DI_{high}$$
$$L\frac{\partial ic}{\partial t} = D(V_{low} - i_L(rL + rs))$$

$$\dot{X} = Ax + BU$$
$$\dot{Y} = Cx + EU$$

$$U = \begin{bmatrix} V_{low} \\ I_{high} \end{bmatrix}, X = \begin{bmatrix} i_L \\ V_c \end{bmatrix}$$

$$A = DA_1 + D^{'}A_2 = \begin{bmatrix} -\frac{rc + rs + D^{'}rc}{L} & -\frac{D^{'}}{L} \\ \frac{D^{'}}{C} & 0 \end{bmatrix}$$

$$B = DB_1 + D^{'}B_2 = \begin{bmatrix} \frac{1}{L} & -\frac{D^{'}rc}{L} \\ 0 & -\frac{1}{C} \end{bmatrix}$$

$$C = DC_1 + D^{'}C_2 = \begin{bmatrix} D^{'}rc & 1 \end{bmatrix}$$

$$E = DE_1 + D^{'}E_2 = \begin{bmatrix} 0 & -rc \end{bmatrix}.$$

This state space model is derived from the small signal model method, which considers two cases: switch on and off, then combine those two equations about inductor current and capacitor voltage together. D=1-D’.

In all, the state space model of each power stage is calculated and presented. It can be used for controller design or system stability analysis. The following chapter is mainly based on the accepted conference paper content [42].

5. LARGE SIGNAL STABILITY ANALYSIS OF A HYBRID AC/DC MICROGRID WITH A CASCADED CONTROL INVERTER

5.1 Introduction

With ever improving applications of renewable energy sources, the framework of traditional power systems is gradually changing. One typical example is the emergence of various microgrids, which act as an interface of renewable energy sources and the utility grid. A microgrid can be regarded as a subsystem affiliated to a normal utility grid without considering working modes, which handles problems like stability, control, and power management in the integration of renewable energy sources. Based on the involved electricity bus [35][36], the microgrid is classified into three types: AC microgrid, DC microgrid, and hybrid AC/DC microgrid. For AC microgrid, all the energy sources, loads, and other energy storage systems are connected through the point of common coupling [35]. DC microgrid is constructed based on a stable DC link, and all the energy sources and loads are connected to the same DC bus. The DC link is then integrated with the utility grid via a bidirectional DC-AC inverter. Hybrid AC/DC microgrid consists of both stable AC and DC buses.

The stability of microgrid needs to be guaranteed before various applications. Microgrid stability can be generally classified into two categories based on different working conditions, grid-connected and islanded. Each one has small disturbance stability and transient stability issues [25]. Typically, the small disturbance and transient stability of grid-connected microgrid only involve voltage stability. However, the islanded microgrid stability concerns both voltage and frequency stability. There are many aspects of analyzing the microgrid stability (e.g., control strategy, load and fault type)[26].

Considering the analysis method, small signal and large signal analysis are the two main strategies.

Small signal stability analysis first linearizes a nonlinear system at a specific operation point. Once the linearized system model is obtained, linear stability analysis tools can then be applied to analyze the system stability. Routh-Hurwitz stability criterion, eigenvalue and sensitivity analysis, or Nyquist were the commonly used methods [17][18]. Small signal perturbation method was also largely used in small signal stability analysis [18]. Small signal models for inverters [19], rectifiers [20], and converters [21] were developed specifically for microgrid stability and operation analysis. Although the small signal stability could be verified under a specific local linearization domain, the limitations of operation points were not defined [17][22].

On the other hand, large signal stability is less discussed for microgrid, which is directly based on nonlinear mathematical models without linearization. Lyapunov-based stability analysis methods were commonly used to find the estimated domain of attraction [23][24], which was understood as estimated stability region around a stable operation point [17]. Previous research considering the stability of a DC/AC inverter connected to the infinite grid bus depended on a droop-controller and did not combine the DC bus dynamics with AC grid dynamics together [24]. For example, only the DC bus dynamics was discussed, and AC was treated as a load requirement in [23]. This paper integrates the DC link stability and AC grid stability together based on a cascade controller and different plant parameters.

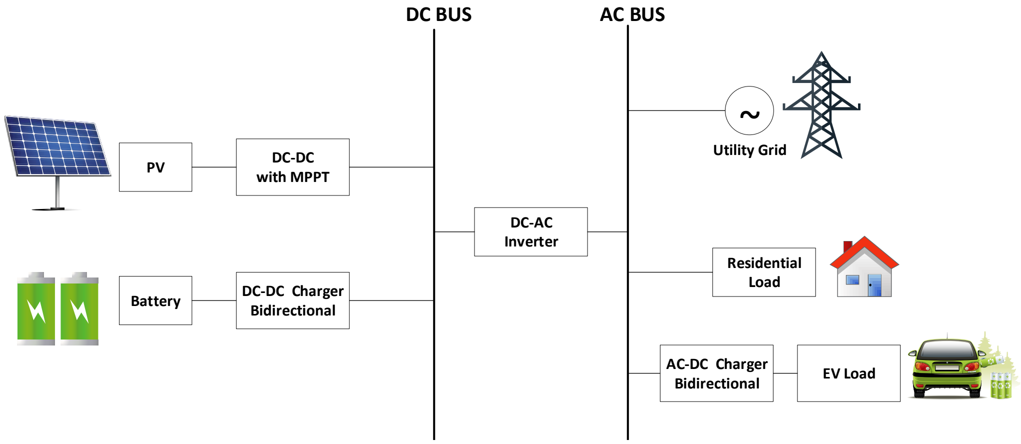

Figure 36. Schematic of the microgrid.

In this thesis, the study of the large signal stability on the input and output side (DC link dynamics and LCL filter dynamics) of the inverter is based on the proposed household hybrid AC/DC microgrid, shown in Figure 36. In this microgrid configuration, a PV connected to the DC bus is assumed to be always working at the maximum power point controlled by a DC-DC converter. Battery storage is connected to the DC bus. The home appliance load and EV battery are powered by the AC bus. Hence, the common droop control, which mainly focuses on power-sharing strategy, is not suitable for the proposed inverter system working mode. In other words, since the proposed household microgrid has a relatively low power input from the PV, it is rare that the PV input power is higher than the microgrid power demand. Thus, different from the previous large-signal stability analysis on a droop-controlled inverter [24], this paper considers a different working scenario with a different control strategy, which analyzes both AC and DC side dynamics together. First, a nonlinear mathematical model of a PI and PR (proportional resonant) cascaded controlled inverter is developed. Then, nonlinear functions, which represent nonlinearities of PR and PLL (phase lock loop) controllers, are replaced by their maximum and minimum values in the stability analysis. In the model, both DC and AC dynamics are analyzed together since the cascaded control combines both sides together (the output of voltage controller is the reference of the current controller). Finally, the large signal stability analysis tool [23] is applied to find the estimated stability region. The impacts of system parameters on the stability regions are also discussed. Moreover, the stability region variances for different control parameters are studied. High fidelity PLECS simulation is applied to validate the stability analysis results.

5.2 DC/AC inverter model with both dc bus dynamics and grid side dynamics

Home applied PV microgrid (string inverter) with a DC-DC converter connecting PV with a DC/AC inverter was discussed in the literature [1][12][15]. A PV inverter system has mainly two working modes, grid-connected and stand-alone. This paper focuses on the grid-connected mode with a constant load requirement of the household inverter system, which corresponds to the proposed microgrid schematic in Figure 36. PV panel is controlled to work at the MPPT [16] by a DC-DC converter. The connecting point of converter and inverter is a capacitor with enough capacity, called the DC link [15]. The DC link voltage is supposed to be a stable value in order to guarantee the system works in good condition. To make sure only the active power is delivered from the grid, a specific PR controller and a PLL controller are applied to control the LCL filter current in phase with the utility grid to maintain UPF (Unity Power Factor). Compared with conventional single L filter or LC filter, LCL filter has a better performance of removing the high-frequency current, which is widely applied as a harmonic attenuator. The control logic for the inverter is a cascaded control that the DC link voltage and UPF are controlled only by the inverter, as shown in Figure 37.

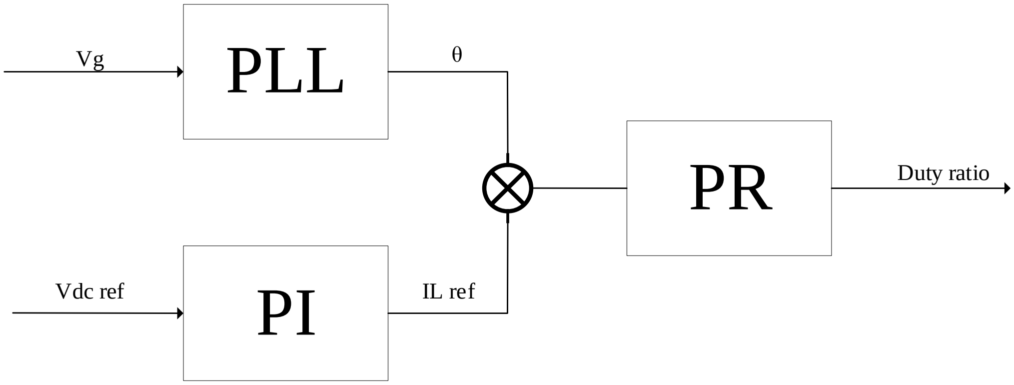

Figure 37. Control logic.

The inverter input, namely the DC link capacitor, is considered as the starting point to analyze the system, and the rest of the grid-connected inverter is also discussed. However, the PV panel dynamics and the boost DC-DC stage are not considered in this paper. The reason is that the duty ratio of the DC-DC boost converter is used to control the PV panel to work at the maximum power point, from which the DC load can always extract the maximum power from PV. Usually, energy storage is introduced to maintain the DC link voltage on island mode. A block diagram of the target system which is part of the proposed microgrid system is shown in Figure 38.

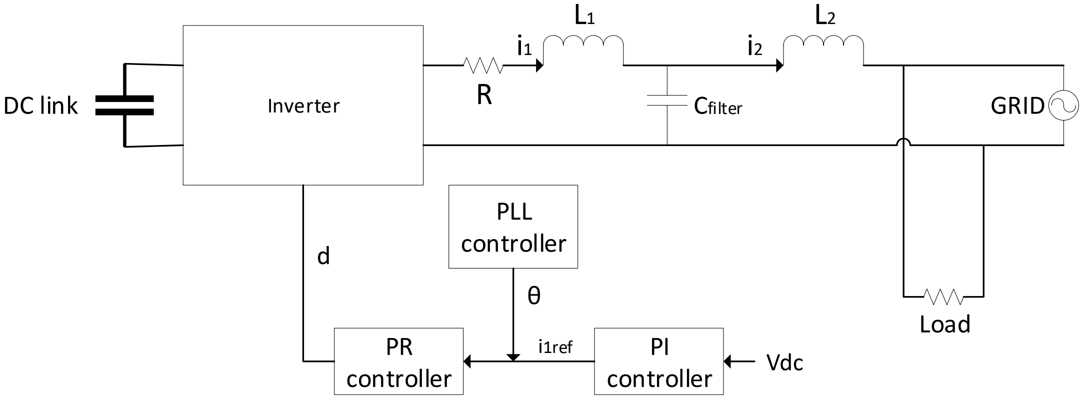

Figure 38. Overall circuit diagram.

The basic LCL filter was applied in a DC/AC microgrid to connect the inverter with the utility grid [27]. Different from a droop controller [28], the PI controller cascaded with PR controller regulates both the DC link voltage and the grid current. Synchronization was achieved through a PLL controller [29]. The PI controller compares the DC link voltage with the real-time voltage value and the output is the grid current reference (peak value of single phase current). The function of PLL controller is mainly to make the grid current in phase with the grid voltage (maintain UPF). With the grid current reference multiplied by phase information (θ), the input of the PR controller is defined. Compared with the grid current that goes through the first inductor in the LCL filter, the output of the PR controller is the switch duty ratio. Thus, the DC link voltage and the grid current can be regulated to the reference values. The outer loop controller is a standard PI controller, which can be substituted by a K-factor controller [30]. As the inner loop controllers, the PR and PLL controllers were discussed in the literature [29][31]. Compared with other existing controllers, this cascaded controller for the inverter system integrates both DC and AC dynamics together. Thus, a large signal Lyapunov-based method is applied to find the operation boundaries.

A new full order droop-controlled DC/AC inverter model, which considered only AC dynamics for stability analysis, was discussed before [24]. For the same LCL filter to the grid system, this paper develops a model that has different control logic and integrates the DC link dynamics with the AC dynamics together.

The nonlinear model of the system above is constructed in the following state-space model,

$$\dot{x} = Ax + Bu \,, \tag{19}$$

where $x = [\mathrm{i}_1 \ \mathrm{V}_c \ \mathrm{i}_2 \ \mathrm{V}_{DC} \ \mathrm{T}_d \ \mathrm{V}_{Cfilter}]^T$, u is the control input of the corresponding state variables. The whole model is typically based on circuit dynamics (mainly capacitor and inductor dynamics). Moreover, Power system like the converter-based system should have the controller to drive the system to work in a stable condition. In this case, the controller dynamics should also be considered when analyzing the system stability. Considering all the dynamics together, the proposed model is constructed as the nonlinear state-space model. The matrix A has nonlinearities in it.

For large signal stability analysis, there are different analysis tools [23]. For example, the multi-model approach utilizes Takagi-Sugeno (TS) multi-modeling to approximate a nonlinear system. By solving the corresponding Linear Matrix Inequalities (LMIs), a Lyapunov energy function for the nonlinear system is then found to estimate stability regions. Other methods include Brayton-Moser's mixed potential [37], BDQLF (Block diagonalized quadratic Lyapunov function) method [38], reverse trajectory tracking method [39]. In this paper, the multi-model approach using TS multi-modeling is applied to construct the desired linear dynamic model. In stability analysis, the state space model is usually transformed to an error model, which is constructed in the steady state condition. Since the state references in a stable operating condition are also constant, the derivative of the error state variable Δx is equal to the state derivative of x. Note that V_{DCref} for the DC link is a desired value depending on the application, which is assumed a constant value in this paper. Consequently, all the other references are calculated through the known controller and dynamic equations. Thus, the new model with error state variables is expressed as follows.

$$\dot{x}^* = A \cdot x^*, \tag{20}$$

where
$$x^* = [\Delta \mathrm{i}_1 \;\; \Delta \mathrm{V}_c \;\; \Delta \mathrm{i}_2 \;\; \Delta \mathrm{V}_{DC} \;\; \Delta T_d \;\; \Delta \mathrm{V}_{Cfilter}]^T$$
$$\Delta \mathrm{i}_1 = \mathrm{i}_1 - \mathrm{i}_{1ref}, \Delta \mathrm{V}_c = \mathrm{V}_c - \mathrm{V}_{cref}, \Delta \mathrm{i}_2 = \mathrm{i}_2 - \mathrm{i}_{2ref},$$
$$\Delta \mathrm{V}_{DC} = \mathrm{V}_{DC} - \mathrm{V}_{DCref}, \Delta T_d = T_d - \mathrm{T}_{dref},$$
$$\Delta \mathrm{V}_{Cfilter} = \mathrm{V}_{Cfilter} - \mathrm{V}_{Cfilter\ ref}$$

For the proposed model, the following equations are used to calculate the A matrix, where the ESR of the filter capacitor in LCL is negligible.

$$\begin{cases} L_1 \cdot \dot{i}_1 = V_{inv} - (i_1 \cdot R + V_{cfilter}) \\ L_2 \cdot \dot{i}_2 = V_{cfilter} - V_g \\ C_{filter} \cdot \dot{V}_{cfilter} = i_1 - i_2 \end{cases}, \tag{21}$$

The equations in (21) describe the dynamics of the LCL filter. V_{inv} is the output of the inverter, i_1 and i_2 are the currents through the first and second inductor respectively. V_g denotes the grid voltage. $V_{cfilter}$ is the filter capacitor voltage. The three states (i_1, i_2 and $V_{cfilter}$) are derived from the three equations above.

PR controller is described as,

$$\begin{cases} i_1 \cdot G_{PR} = V_c \\ G_{PR} = K_p + K_R s \big/ \left(s^2 + \omega^2\right) \end{cases}, \tag{22}$$

where V_c denotes the control voltage of the inverter that can be regarded as the duty ratio. ω is the grid frequency. K_P and K_R are the controller parameters. The state V_c is derived from the above equations combined with the system equations (24).

PI controller is shown as,

$$\begin{cases} V_{DC} \cdot G_{PI} = i_1 \\ G_{PI} = K_{P1} + K_I / s \\ \dot{T}_d = V_{DC} \end{cases}, \tag{23}$$

where V_{DC} denotes the state of DC link voltage, K_{P1} and K_I are the controller parameters, where T_d is the auxiliary state variable introduced for describing the integrator part of PI controller when the first two equations are combined together. The state V_{DC} and T_d are derived from the above equations combined with the system equations (24).

The other system dynamics in Figure 38 are shown below,

$$\begin{cases} C_{filter} \cdot \dot{V}_c = \dfrac{i_1}{V_{dc}} - \dfrac{i_2}{V_{dc}} \\ V_c \cdot V_{dc} = V_{cfilter} \\ \dot{V}_{dc} = \dfrac{V_{ac}}{C_{dc} \cdot V_{dc}} \cdot i_1 \end{cases} . \tag{24}$$

The dynamic of V_c is derived by substituting the second equation in (21) to the filter voltage dynamics equation. The equations above are based on the inverter input and output relationship and power matching condition. The derivation of V_c dynamics with approximations is shown in the second part of Appendix A. V_{dc} is the desired stable value of DC bus.

Integrate all the system equations above, the final model is written as,

$$\dot{x}^* = A^* \cdot x^* , \tag{25}$$

where,

$$A^* = \begin{bmatrix} -\dfrac{R}{L_1} & 0 & 0 & 0 & 0 & -\dfrac{1}{L_1} \\ 0 & \dfrac{1}{C_{filter} V_{dc} f_1(x) f_2(x)} & -\dfrac{1}{C_{filter} V_{dc}} & 0 & 0 & 0 \\ 0 & 0 & 0 & 0 & 0 & \dfrac{1}{L_2} \\ 0 & 0 & 0 & \dfrac{V_{ac}}{C_{dc} V_{dc}} K_p & \dfrac{V_{ac}}{C_{dc} V_{dc}} K_i & 0 \\ 0 & 0 & 0 & 1 & 0 & 0 \\ \dfrac{1}{C_{filter}} & 0 & \dfrac{-1}{C_{filter}} & 0 & 0 & 0 \end{bmatrix} ,$$

$f_2(x)$ is the transfer function G_{PR} and $f_1(x)$ (θ) is the output of the PLL controller. System nonlinearities are embedded in functions $f_1(x)$ and $f_2(x)$, respectively.

5.3 Estimated domain of attraction

The basic idea of the large signal stability analysis, based on the TS multi-modeling, is that the nonlinear system mathematical equations is first written into the state space model $\dot{x} = Ax$. The input of the autonomous system is zero since the system is analyzed around an equilibrium point, which is typically the origin after shifting with reference signals in the error dynamics. For nonlinearities in A the matrix, each nonlinearity will be calculated as the minimum and maximum values. Thus, multiple A matrices are constructed based on different boundary values, which represents that multiple linear system matrices are derived by setting the upper and lower boundaries. These matrices are combined to construct a M matrix for calculating the Lyapunov system energy function, which is utilized to estimate the system stable regions [23]. The Lyapunov function is derived by solving the following Linear Matrix Inequalities (LMIs).

$$\begin{cases} M = M^T > 0 \\ A_i^T * M + M * A_i < 0 \end{cases}, \tag{26}$$

where the A_i matrix is defined by the boundaries of nonlinear functions, $f_1(x)$ and $f_2(x)$. The maximum and minimum values of the two nonlinear functions are found in the following. For the PLL controller, nonlinearity is defined as,

$$0 < f_1(x) = \theta < \pi, \tag{27}$$

The nonlinearity of PR controller is regarded as,

$$\min < f_2(x) < \max, \tag{28}$$

where the minimum and maximum values are calculated through the NIKE function characteristics since the function $f_2(x)$ has the same format as the standard NIKE function. Moreover, these two nonlinearities are in the same element of the matrix A, which can be calculated as one lumped pair of maximum and minimum values.

Thus, the M matrix in (26) is calculated by solving LMIs. Once the M matrix is obtained, the Lyapunov candidate function for analyzing the large signal stability of the system is constructed by,

$$V(x) = x^{*T} \cdot M \cdot x^{*} . \tag{29}$$

Since the developed system has six different variables, it is not intuitive to plot all the variables together in one phase plot. For demonstration, the parameters i_1 and V_{dc} are selected for the following simulation and discussions, which represent the LCL filter inductor (AC side) and the DC link capacitor (DC side) dynamics, respectively.

5.4 Simulation results and discussions

The system parameters for simulation are shown in Table 4

Table 4. System parameter for large signal stability analysis.

R (ohm)	0.01	C_{filter} (F)	1.15e-5
L_1 (H)	3.18e-3	V_{ac} (V)	24(peak)
L_2 (H)	1.91e-3	V_{dc} (V)	30
C_{dc} (F)	3e-3	f (HZ)	60
K_p	1	$f_1(x)$	[-0.3,2.29]
K_i	1	$f_2(x)$	[0,π]

For a normal string inverter system, the desired system output power extracted from the PV panel is around 1 kW to 5 kW. In that case, the PV output and the corresponding DC link voltage and grid voltage will be relatively high. For the large signal stability analysis in this paper, the DC link voltage is controlled at 30V, and the grid voltage is 24V (peak) 60Hz. Thus, this kind of scaled down system is easy to be analyzed and implemented in a prototype microgrid. All the other parameters are calculated based on the system requirement. When the parameters are used to derive the A matrix, a scale factor of 1000 is chosen to make the stability region more reasonable and relevant to real simulation results. The PI controller parameters are set as 0.3 to achieve the control goal. The frequency of the grid is 60 Hz. The nonlinear function $f_1(x)$ that represents the PR controller transfer function has a range from -0.3 to 2.29. Finally, the PLL controller for the inverter grid synchronization is varied from 0 to π. The load size on the grid side is set to 2 ohms for simulation verification. With the set of parameters in Table 4. The system stability analysis is discussed as follows.

5.4.1 Case 1: Evaluation of the DC link capacitor.

The large stability analysis based on six parameters of the system is presented in the x_1 and x_2 frame, which are the inductor current and the DC link voltage, respectively. The steady state condition is aimed to work in the desired condition (mainly V_{dc} equals to 30 V, inverter output in phase with the grid (UPF)). Under this normal operation condition, the impact of the DC link capacitor capacity on the stability margin of the DC link voltage is first explored.

The Lyapunov-based asymptotic stable domain of attraction is presented in Figure 39. The result shows that increasing the capacitor capacity will also enlarge the voltage margins. However, the maximum current region, which is x_1 in the figure, remains the same. The reason is that output from PV is a constant value (MPPT), corresponding to a fixed grid voltage region. Thus, the maximum current should be no more than the calculated one. The capacitor is chosen to vary from 1 mF to 3 mF. Meanwhile, the inductor value is set to be a constant value at 1 mH. The range of the margin changes from around 60V to 80V. From large-signal stability analysis perspective, this means that for controlling the system to a higher desired voltage, the larger capacitor will lead the system margin to a higher level. In other words, the system will oscillate or even become unstable if the control goes beyond the value that the capacitor can hold

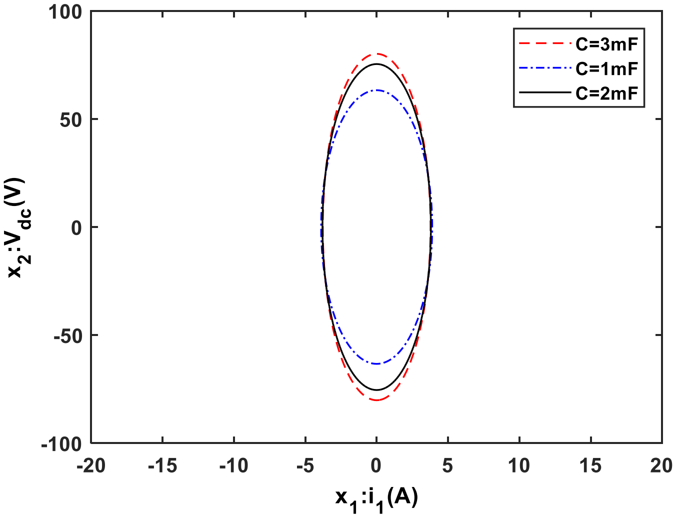

Figure 39. Estimated region changes with different DC link capacitor values.

To validate the large signal stability region above, the PLECS simulation of the circuits is tested to explore the system stability boundary. The first simulation parameter is 1 mF (capacitor value). In Figure 40. The result shows the value of the DC link voltage is around 63V, which is maximum value that the system can hold. When the reference voltage is set beyond 63V, the DC link voltage will have a high oscillation. The simulation results show that the estimated region of stability is confirmed. The estimated stability region of the Lyapunov method is more conservative compared to the PLECS simulation results.

The second simulation is tested for the capacitor is 3 mF. The estimated stability boundary is around 80V. The simulation result is shown in Figure 41. The voltage reference is set as a step change from 71V to 80V, and the response shows that the system can work in a stable way. When the reference is chosen to be more than 80V, the system will become unstable. In Figure 42. Results show that the system starts to oscillate and the simulation is unable to continue around 0.03 second. Thus, the system boundary increase matches with the estimation results.

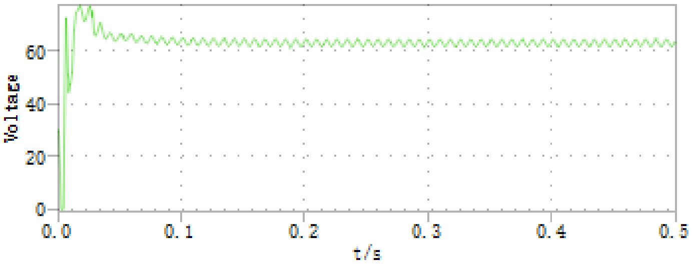

Figure 40. Simulation results. (Cdc=1mF)

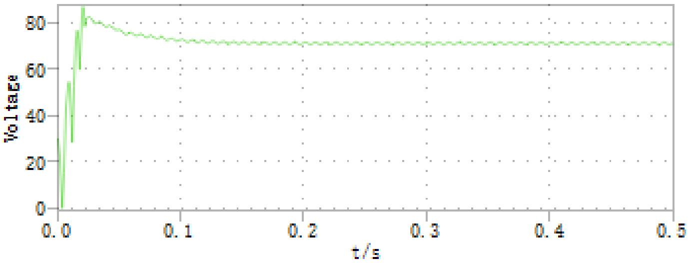

Figure 41. Simulation results. (Cdc=3mF)

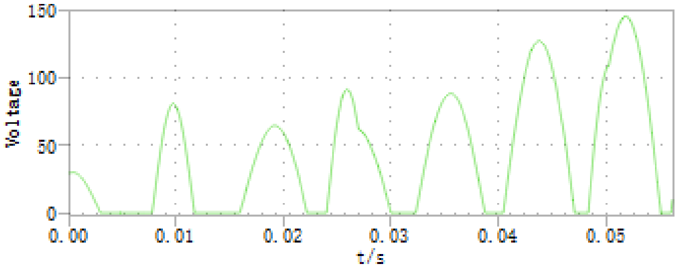

Figure 42. The system becomes unstable. (reference exceeds the limit)

5.4.2 Case 2: Evaluation of the LCL filter inductor

In Figure 43, another estimated domain of attraction is presented, which aims to explore the influence of different grid inductor values on the DC link voltage stability. In this figure, three different values of the inductor, 0.6 mH, 1 mH, and 3 mH, are applied respectively, and all the other system parameters remain the same. For the largest inductor value (3mH), the boundary is around 62 V that is shown as the smallest green ellipse. As the first inductor value in the LCL decreases, the estimated attractions based on the large signal Lyapunov method increases. For the lowest value inductor 0.6 mH, the stability boundary is close to 85V. The result shows that the DC link stability region of the cascaded control-based inverter will be enlarged if the inductor value is chosen to be a smaller value. However, the value must be within a reasonable range when designing the LCL filter. Moreover, in Figure 43, it is shown that changing the inductor value of the grid side will have some impacts on the DC link stability. The effect of the inductor changes will become relatively not remarkable as the inductor capacity drops to a low value.

Two PLECS simulation results are presented to verify the above-estimated stability regions. The DC link capacitor value is set to be 3 mF. Choosing the inductor value to be 1.1 mH, the maximum value of the DC link voltage is around 80 V, shown in Figure 44. A step change of voltage reference is set to explore the stability of the system. Results show that the maximum value the simulation can hold is around 80V. Finally, the inductor value is set to 3 mH, and the PLECS simulation results show that the stability boundary is around 60V. The estimated region is around 58V, which matches with the analysis result. When the reference value is set to more than the boundary value in this situation, the system will be unstable shown in Figure 45. High voltage oscillations occur between 0V to 30V. The criteria for defining the system is stable or not in PLECS is to find if the voltage will reach the reference value. Moreover, if the DC link voltage encounters high oscillations, this is also considered unstable.

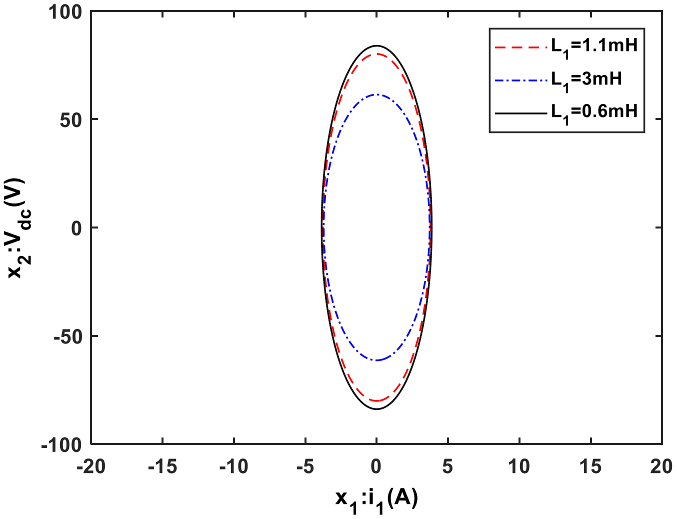

Figure 43. Estimated region changes with different LCL filter inductor values.

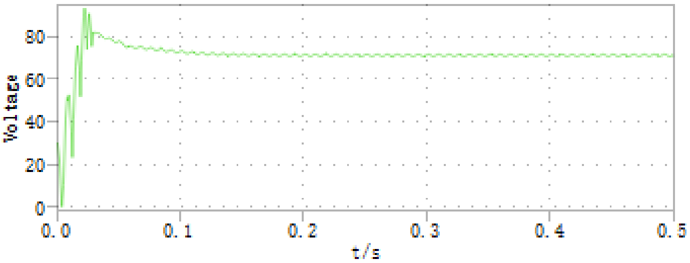

Figure 44. Simulation results. (L1=1.1mH)

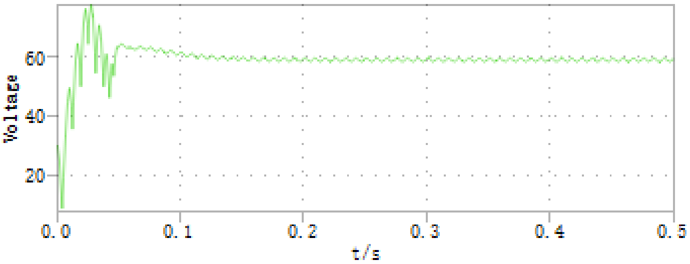

Figure 45. Simulation results. (L1=3mH)

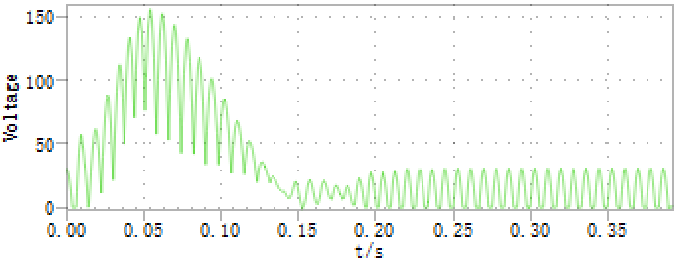

Figure 46. The system becomes unstable. (reference exceeds the limit)

5.4.3 Case 3: Evaluation of the PI controller parameter.

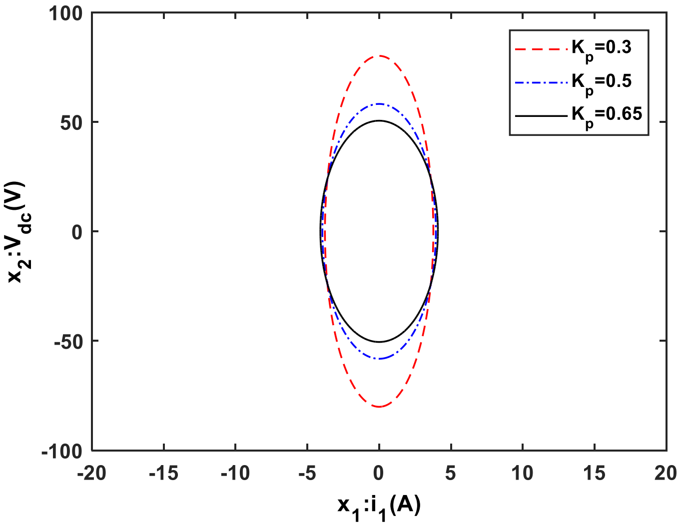

Figure 47. Estimated regions for different control parameter values.

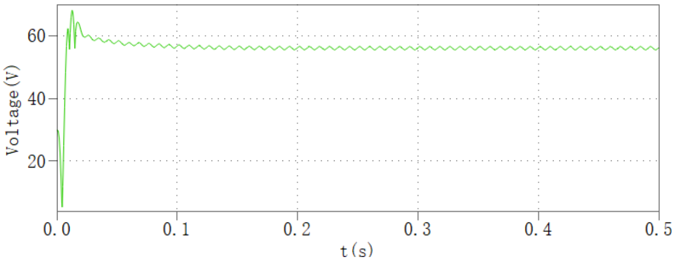

Figure 48. PLECS simulation results (Kp=0.5).

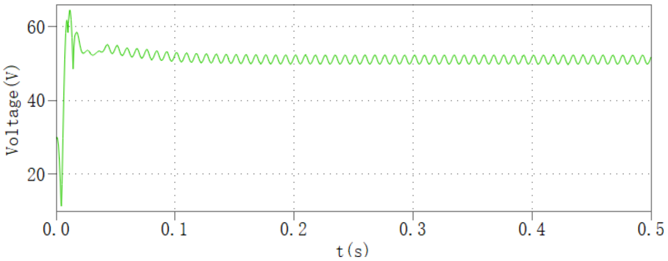

Figure 49. PLECS simulation results (Kp=0.65).

In Figure 47, the effects of the various controller parameters are explored, which aims to study how the controller parameters influence the stability regions. Three different proportional gains are chosen as 0.3, 0.5 and 0.65 to get the estimated domains of attraction. All the other system parameters remain the same. For the largest value Kp=0.65, the maximum dc link voltage is around 40V. As the proportional gain, Kp decreases to 0.5 and 0.3, the maximum voltage value actually increases to 56V and 80V, respectively. The results show that as the controller parameter (Kp) increases, the corresponding stability boundary will decrease. A larger proportional gain will result in a larger change in response to the same error, and the system is easier to encounter highly oscillations, which means the larger the proportional gain, the smaller the estimated stability boundaries.

Simulations are implemented in PLECS to validate the estimation results. In Figure 48, the stability boundary for Kp=0.5 is presented. The maximum value that the simulation voltage can be set is around 59V, which is similar to the estimated result. For the bigger controller parameter value (Kp=0.65), the maximum voltage is around 50V, which is shown in Figure 49. This means the estimated boundary is a little bit conservative than the real simulation result. Both PLECS simulation results and the Lyapunov stability region estimation illustrate the fact that bigger controller parameters will cause the stability region to become narrower.

Three different cases validate the estimated domain of attraction through PLECS simulation. The simulation results are based on a PV string inverter microgrid schematic, which can be regarded as a household application PV system. This study confirms that the Lyapunov-based large-signal stability analysis method can be utilized as a tool to estimate the stability boundary. Although the results will not be exact as the PLECS simulation results, it can serve as a reference or an indicator.

5.5 Conclusion

The large signal stability of the scaled down grid-connected inverter in a PV home application is explored. The nonlinear dynamic system model is developed. The effects of different DC link capacitors and the impact of grid side inductors on DC side are discussed. Simulation results of PLECS software are applied to verify the estimated stability regions.

Both the simulation results and the estimated large-signal stability regions show that a larger DC link capacitor will enhance stability regions. Moreover, the influence of the grid inductor on the DC link stability is not negligible. The inductor with a bigger value will reduce the estimated stability regions. In addition, a larger proportional control value will shrink the system stability region.

5.6 Future work

Future work should concentrate on exploring whether Lyapunov stability region should be conservative than the real simulation results or not. Moreover, in this proposed model, both PR controller and PLL controller are regarded as nonlinear functions. A suitable modeling method should be applied to study the impact of these two controller parameters on the stability estimated region. Moreover, the stand-alone mode of this kind of system should be modeled as well.

REFERENCES

[1] "IEEE Guide for Design, Operation, and Integration of Distributed Resources Island Systems with Electric power System," in IEEE Std 1547.4-2011, pp. 1-54, July. 20. 2011.

[2] QER 1.2 Appendix A: "Electricity System Overview", Jan.4, 2017

[3] T. A. Short, "Electric Power Distribution Handbook", CRC Press, 2004

[4] J. M. Carrasco, L. G. Franquelo, Bialasiewicz, J. T, Galván, E., PortilloGuisado, R.C., Prats, M.M., León, J.I. and N. Moreno-Alfonso, "Power-electronic systems for the grid integration of renewable energy sources: A survey," IEEE Transactions on industrial electronics, vol. 53, no. 4, pp.1002-1016, 2006.

[5] A. Bidram, V. Nasirian, A. Davoudi, F. L. Lewis, "Cooperative Synchronization in Distributed Microgrid Control," 2017.

[6] H. Sakaguchi, A. Ishigame, and S. Suzaki, "Transient stability assessment for power system via Lur'e type Lyapunov function," In Power Systems Conference and Exposition, 2004. IEEE PES (pp. 227-232). IEEE, October, 2004.

[7] S. Rosado, R. Burgos, F. Wang and D. Boroyevich, "Large-signal stability assessment of AC/DC systems with multi-pulse rectification and DC-fed PWM motor drives," In Power Electronics Specialists Conference, 2007. PESC 2007. IEEE (pp. 2168-2173). IEEE, June, 2007

[8] T. Takagi, and M. Sugeno, "Fuzzy identification of systems and its applications to modeling and control," In Readings in Fuzzy Sets for Intelligent Systems (pp. 387-403), 1993.

[9] J. Willems, "Direct method for transient stability studies in power system analysis," IEEE Transactions on Automatic Control, vol. 16, no. 4, pp.332-341, 1971.

[10] K. L. Praprost and K. A. Loparo, "An energy function method for determining voltage collapse during a power system transient," IEEE Transactions on Circuits and Systems I: Fundamental Theory and Applications, vol. 41, no. 10, pp.635-651, 1994.

[11] F. S. Prabhakara and A. H. El-Abiad, "A simplified determination of transient stability regions for Lyapunov methods," IEEE Transactions on Power Apparatus and Systems, vol. 94, no. 5, pp.672-689, 1975.

[12] S. B. Kjaer, J. K, Pedersen and F, Blaabjerg, “A review of single-phase grid-connected inverters for photovoltaic modules,” IEEE transactions on industry applications, vol. 41, no. 5, pp.1292-1306, 2005.

[13] T. Kerekes, R. Teodorescu, M. Liserre, C. Klumpner and, M. Sumner, “Evaluation of three-phase transformerless photovoltaic inverter topologies,” IEEE Transactions on Power Electronics, vol. 24, no. 9, pp.2202-2211, 2009.

[14] R. González, E. Gubía, J. López and L. Marroyo, “Transformerless single-phase multilevel-based photovoltaic inverter,” IEEE Transactions on Industrial Electronics, vol. 55, no. 7, pp.2694-2702, 2008.

[15] Q. Li, and P. Wolfs, “A review of the single phase photovoltaic module integrated converter topologies with three different DC link configurations,” IEEE Transactions on Power Electronics, vol. 23, no. 3, pp.1320-1333, 2008.

[16] A. R. Reisi, M. H. Moradi and S. Jamasb, “Classification and comparison of maximum power point tracking techniques for photovoltaic system: A review,” Renewable and Sustainable Energy Reviews, vol. 19, pp.433-443, 2013.

[17] M. Kabalan, P. Singh and D. Niebur, “Large signal Lyapunov-based stability studies in microgrids: A review,” IEEE Transactions on Smart Grid, vol. 8, no. 5, pp.2287-2295, 2017.

[18] P. Kundur, N. J. Balu and M. G. Lauby, “Power system stability and control,” Vol. 7. New York: McGraw-hill, 1994.

[19] F. Katiraei, M. R. Iravani and P. W. Lehn, “Micro-grid autonomous operation during and subsequent to islanding process,” IEEE Transactions on power delivery, vol. 20, no. 1, pp.248-257, 2005.

[20] N. Bottrell, M. Prodanovic and T. C. Green, “Dynamic stability of a microgrid with an active load,” IEEE Transactions on Power Electronics, vol. 28, no. 11, pp.5107-5119, 2013.

[21] G. N. Love and A. R. Wood, December, “Small signal model of a power electronic converter,” In Power Engineering Conference, IPEC 2007. International (pp. 636-642). IEEE, 2007.

[22] P. Kundur, J. Paserba, V. Ajjarapu, G. Andersson, A. Bose, C. Canizares, N. Hatziargyriou, D. Hill, A. Stankovic, C. Taylor and T. Van Cutsem, "Definition and classification of power system stability IEEE/CIGRE joint task force on stability terms and definitions," IEEE Transactions on Power Systems, vol. 19, no. 3, pp.1387-1401, 2004.

[23] D. Marx, P. Magne, B. Nahid-Mobarakeh, S. Pierfederici and B. Davat, “Large signal stability analysis tools in DC power systems with constant power loads and variable power loads—A review,” IEEE Transactions on Power Electronics, vol. 27, no. 4, pp.1773-1787, 2012.

[24] M. Kabalan, P. Singh and D. Niebur, “Large signal stability analysis of a DC/AC droop controlled inverter connected to an infinite bus,” In North American Power Symposium (NAPS), (pp. 1-6). IEEE, October, 2015.

[25] Z. Shuai, Y. Sun, Z. J. Shen, W. Tian, C. Tu, Y. Li and X. Yin, “Microgrid stability: Classification and a review,” Renewable and Sustainable Energy Reviews, vol. 58, pp.167-179, 2016.

[26] R. Majumder, “Some aspects of stability in microgrids,” IEEE Transactions on power systems, vol. 28, no. 3, pp.3243-3252, 2013.

[27] A. E. W. H. Kahlane, L. Hassaine and M. Kherchi, "LCL filter design for photovoltaic grid-connected systems," the Journal of Renewable Energies, pp.227-232, 2014.

[28] F. Katiraei and M. R. Iravani, “Power management strategies for a microgrid with multiple distributed generation units,” IEEE transactions on power systems, vol. 21, no. 4, pp.1821-1831, 2006.

[29] L. G. B. Rolim, D. R. da CostaJr and M. Aredes, “Analysis and software implementation of a robust synchronizing PLL circuit based on the pq theory,” IEEE Transactions on Industrial Electronics, vol. 53, no. 6, pp.1919-1926, 2006.

[30] A. Vangari, D. Haribabu and J. N. Sakamuri, “Modeling and control of DC/DC boost converter using K-factor control for MPPT of solar PV system,” In Energy Economics and Environment (ICEEE), International Conference (pp. 1-6), March, 2015.

[31] H. Cha, T. K. Vu and J. E. Kim, “Design and control of Proportional-Resonant controller based Photovoltaic power conditioning system,” In Energy Conversion Congress and Exposition, IEEE (pp. 2198-2205), September, 2009.

[32] R. J. Wai, W. H. Wang and C. Y. Lin, “High-performance stand-alone photovoltaic generation system,” IEEE Transactions on Industrial Electronics, vol. 55, no. 1, pp.240-250, 2008.

[33] S. Daher, J. Schmid and F. L. Antunes, “Multilevel inverter topologies for stand-alone PV systems,” IEEE transactions on industrial electronics, vol. 55, no. 7, pp.2703-2712, 2008.

[34] J. Zhang, “Bidirectional DC-DC power converter design optimization, modeling and control,” (Doctoral dissertation, Virginia Tech), 2008.

[35] E. Planas, J. Andreu, J. I. Gárate, I. M. de Alegría, and E. Ibarra, “AC and DC technology in microgrids: A review,” Renewable and Sustainable Energy Reviews, vol. 43, pp.726-749. 2015.

[36] H. Lotfi, and A. Khodaei, “AC versus DC microgrid planning,” IEEE Transactions on Smart Grid, vol. 8, no. 1, pp.296-304, 2017.

[37] R. K. Brayton and J. K. Moser, “A theory of nonlinear networks, Part I,” Quart. Appl. Math., vol. 12, no. 1, pp. 1–33, 1964.

[38] C. J. Sullivan, S. D. Sudhoff, E. L. Zivi, and S. H. Zak, “Methods of optimal Lyapunov function generation with application to power electronic converters and systems,” in Proc. IEEE Electric Ship Technol. Symp.,2007, pp. 267–274.

[39] A. Bacha, H. Jerbi, and N. B. Braiek, “An approach of asymptotic stability domain estimation of discrete polynomial systems,” in Proc. IMACS Multiconf. Comput. Eng. Syst. Appl., Oct. 2006, pp. 288–292.

[40] Y. C. Kuo and T. J. Liang, “Novel Maximum-Power-Point-Tracking Controller For Photovoltaic Energy Conversion System,” IEEE Trans. on Industrial Electronics, vol. 48, no. 3, 2001, pp. 594 - 601.

[41] “Tutorial on Power Electronics for PV Power Systems Integration”, ISIE 2010, 4 July 2010, Bari.

[42] Hongru Xu, Yan Chen, and Brian Keel, “Large signal stability analysis of a hybrid AC/DC microgrid with a cascaded control inverter,” *2018 ASME Dynamic Systems and Control Conference*, (Accepted), 2018.

APPENDIX

MATLAB CODE FOR SOLVING PARAMETER A

```
Isc=8.68; Voc=37.5; Ns=60; Vmp=30.2; Imp=8.13; dV_dI_oc=-0.385; Rsh=237;
q=1.6*10^-19;k=1.38*10^-23; T=298;
VT = [];
Io = [];
Rs = [];
Imp_c = [];
n = 1;
for i = 1:0.001:1.5
        aaa(n) = i;
        n = n+1;
end

for i = 1:1:length(aaa)
        VT(i) = (aaa(i)*k*T*Ns)/q;
        Io(i)=Isc/(exp(Voc/VT(i))-1);
        Rs(i)=-dV_dI_oc-VT(i)/Isc;
        Imp_c(i)=Isc-Io(i)*(exp((Vmp+Imp*Rs(i))/VT(i))-1)-(Vmp+Imp*Rs(i))/Rsh;
end

for i = 1:1:length(aaa)
        if Imp_c(i) > Imp
                result = i;
                finalVT = VT(i);
                finalIo = Io(i);
                finalRs = Rs(i);
                finalImp = Imp_c(i);
        end
```

The derivations of V_c dynamics is described as follows.

$$C_{filter} \cdot \frac{\mathrm{d}(V_c \cdot V_{dc})}{\mathrm{dt}} = i_1 - i_2$$

$$C_{filter} \cdot (\dot{V}_c \cdot V_{dc} + V_c \cdot \dot{V}_{dc}) = i_1 - i_2$$

$$C_{filter} \cdot (\dot{V}_c \cdot V_{dc}) + C_{filter} \frac{V_{ac} \cdot V_c}{C_{dc} \cdot V_{dc}} \cdot = i_1 - i_2$$

$$C_{filter} \cdot (\dot{V}_c \cdot V_{dc}) = i_1 \cdot (1 - C_{filter} \cdot \frac{V_{ac} \cdot V_c}{C_{dc} \cdot V_{dc}}) - i_2$$

Since $C_{filter} \cdot \frac{V_{ac} \cdot V_c}{C_{dc} \cdot V_{dc}}$ is negligible compared with 1, the final V_c dynamics is written as,

$$\dot{V}_c = \frac{i_1 - i_2}{C_{filter} \cdot V_{dc}} \text{.}$$

which is the same as that in (24).